Moving magnetoencephalography towards real-world applications with a wearable system

Elena Boto[1+], Niall Holmes[1+], James Leggett[1+], Gillian Roberts[1+], Vishal Shah[3], Sofie S. Meyer[2,4], Leonardo Duque Muñoz[2], Karen J. Mullinger[1,6], Tim M. Tierney[2], Sven Bestmann[2,5], Gareth R. Barnes[2+], Richard Bowtell[1+] and Matthew J. Brookes[1+*]

[+] **Denotes authors who contributed equally to this work**

[1] *Sir Peter Mansfield Imaging Centre, School of Physics and Astronomy, University of Nottingham, University Park, Nottingham, NG7 2RD, United Kingdom*

[2] *Wellcome Centre for Human Neuroimaging, UCL Institute of Neurology, University College London, 12 Queen Square, London, WC1N 3BG, United Kingdom*

[3] *QuSpin Inc., 331 South 104th Street, Suite 130, Louisville, Colorado, 80027, USA*

[4] *Institute of Cognitive Neuroscience, University College London, 17-19 Queen Square, London, WC1N 3AZ, United Kingdom*

[5] *Sobell Department for Motor Neuroscience and Movement Disorders, UCL Institute of Neurology, University College London, Queen Square House, Queen Square, London, WC1N 3BG, United Kingdom*

[6] *School of Psychology, University of Birmingham, Edgbaston, Birmingham, B15 2TT United Kingdom*

[*]**Correspondence to:**
Dr. M. J. Brookes,
Sir Peter Mansfield Imaging Centre,
School of Physics and Astronomy,
University of Nottingham,
University Park,
Nottingham NG7 2RD
E-mail: **matthew.brookes@nottingham.ac.uk**

Summary

Imaging human brain function with techniques such as magnetoencephalography[1] (MEG) typically requires a subject to perform tasks whilst their head remains still within a restrictive scanner. This artificial environment makes the technique inaccessible to many people, and limits the experimental questions that can be addressed. For example, it has been difficult to apply neuroimaging to investigation of the neural substrates of cognitive development in babies and children, or in adult studies that require unconstrained head movement (e.g. spatial navigation). Here, we develop a new type of MEG system that can be worn like a helmet, allowing free and natural movement during scanning. This is possible due to the integration of new quantum sensors[2,3] that do not rely on superconducting technology, with a novel system for nulling background magnetic fields. We demonstrate human electrophysiological measurement at millisecond resolution whilst subjects make natural movements, including head nodding, stretching, drinking and playing a ball game. Results compare well to the current state-of-the-art, even when subjects make large head movements. The system opens up new possibilities for scanning any subject or patient group, with myriad applications such as characterisation of the neurodevelopmental connectome, imaging subjects moving naturally in a virtual environment, and understanding the pathophysiology of movement disorders.

Magnetoencephalography[1] (MEG) allows direct imaging of human brain electrophysiology, via measurement of magnetic fields generated at the scalp by neural currents. Mathematical analysis of those fields enables the generation of 3D images showing the formation and dissolution of brain networks in real time. MEG measurements of brain activity are currently made using an array of superconducting sensors placed around the head[1,4]. These cryogenically-cooled sensors have femtotesla (fT) sensitivity, which is needed to detect the weak magnetic fields produced by the brain. Unfortunately, the requirement for cooling means that sensors must be housed within a liquid helium dewar with a vacuum space separating sensors from the scalp. MEG systems are therefore cumbersome (Figure 1a) and sensor positions are fixed in a one-size-fits-all helmet. Any motion of the head relative to the sensors reduces data quality dramatically: even a 5 mm movement can be prohibitive[5]. Further, the brain-to-sensor distance, which is significant in adults (~3 cm), is increased markedly in subjects with small heads, reducing the available signal because the magnetic field decreases with the square of the source-sensor distance. These characteristics make participation in MEG studies challenging for many subject groups, including infants and many patients. They also make the MEG scanner environment unnatural, and limit the experimental paradigms that can be employed. Here, we describe a transformative MEG technology which can be worn on the head during movement. This opens up the possibility for non-invasive mapping of human electrophysiology across all ages and patient groups, with subjects who are free to move and interact with the real world.

At the core of our system is an array of optically pumped magnetometers (OPMs) – magnetic field sensors that rely on the atomic properties of alkali metals. These sensors have seen marked development in recent years[2,3,6-9] and are well suited to MEG measurements[10-16]. In our system, each sensor contains a 3 x 3 x 3 mm^3 glass cell containing ^{87}Rb vapour which is heated to ~150°C. A 795 nm circularly polarised laser beam, tuned to the D1 transition of rubidium, is used to spin-polarise the atoms, and the intensity of laser light transmitted through the cell is detected using a photodiode. In zero magnetic field, the spin magnetic moments align with the beam, and transmission of laser light to the photo diode is maximised. However, a magnetic field perpendicular to the beam causes Larmor precession, rotating the magnetic moments away from alignment. This causes a measurable drop in light transmission. The resulting effect is a zero-field resonance (Figure 1b), which acts as a sensitive magnetic field indicator.

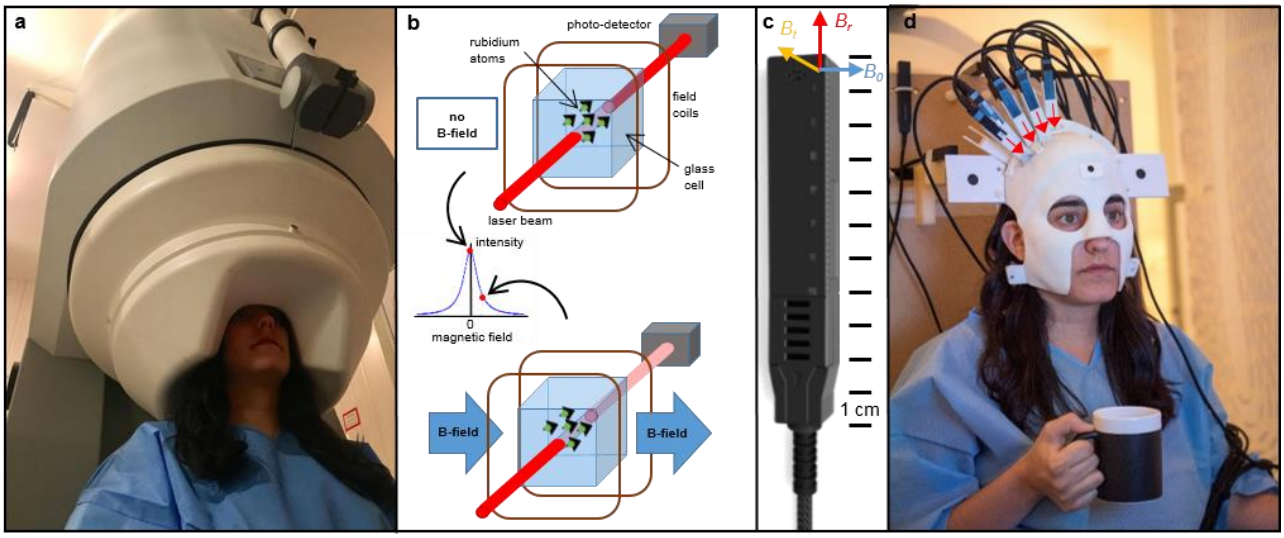

Figure 1: A new generation of MEG system. *a) A conventional 275-channel cryogenic MEG system. Weighing ~450 kg the system is fixed and cumbersome and subjects must remain still relative to the fixed sensor array. b) Schematic illustration of zero-field resonance in an OPM sensor: the upper illustration shows operation in zero-field, the lower illustration depicts Larmor precession when an external field impinges on the cell and the transmitted light intensity is reduced. c) A commercial OPM sensor made by QuSpin. The geometry used is illustrated by the coloured axes where B_r is the radial field component, B_t the tangential field component, and B_O the direction along which the laser beam is orientated. d) Our prototype OPM-MEG system helmet. The helmet weighs 905 g and is customised such that the sensors (which in this prototype only cover right sensorimotor cortex) are directly adjacent to the scalp surface. The subject is free to move their head. The measured radial field direction for the sensors is illustrated by the red arrows.*

Each sensor is an integrated unit (Figure 1c) with a noise level comparable to that of a SQUID (~15 fT/√Hz) and a dynamic range of ±1.5 nT. Although the cell is heated, sensors can be mounted on the scalp because their external surfaces remain close to body temperature. Our prototype system (Figure 1d) comprised an array of sensors which were mounted in a 3D-printed 'scanner-cast'. The scanner-cast[12] was designed using an anatomical MRI scan, such that the internal surface snugly fits the subject's head, whilst the external surface accommodates the OPMs, which were positioned over the right sensorimotor cortex. Four additional reference sensors, sited near the subject's head, were used for background interference measurement.

As a first demonstration, we measured electrophysiological activity in the right sensorimotor cortex during visually-cued abduction of the left index finger. This task robustly elicits a reduction of endogenous beta band (13-30 Hz) oscillations during movement and a rebound (increase above baseline) following movement cessation[17]. Although simple, this task has been applied widely, with

beta modulation being used as a marker of brain plasticity[18,19], psychosis[20,21] and white matter degradation[22]. A single experiment comprised 50 trials, each involving 1 s of finger abduction and 3 s rest. 50 'dummy' trials (where the subject did nothing) were interleaved to allow an estimate of baseline activity. A subject undertook the experiment 12 times: 6 where they kept as still as possible, and 6 where they made natural head movements, including nodding and shaking, stretching and drinking. Head motion was measured using an Xbox Kinect camera, which tracked movement of three fiducial markers on the head. We also undertook the same experiments using a cryogenic MEG system.

Figure 2 shows OPM-MEG data measured when the subject kept still (Figure 2a) and moved (Figure 2b). Subject motion is shown in panel (i). In the static case, motion was less than ±1 cm whereas in the moving case it exceeded ±10 cm. Panel (ii) shows an image[23,24] of beta modulation (pink overlay) whilst panel (iii) shows a time-frequency spectrogram (TFS) of oscillatory change. In the TFS, blue indicates a loss in oscillatory amplitude relative to baseline whereas red indicates an increase. Line-plots of beta amplitude are shown inset. Equivalent data from the cryogenic system are shown in (c), where movement was (necessarily) constrained to <2 mm. OPM-MEG performed consistently across experiments with the characteristic beta decrease and post movement rebound delineated clearly, and localised to sensorimotor cortex. Despite an order of magnitude increase in head movement, there was no significant difference in signal-to-interference ratio (SIR) between the moving and static runs ($p = 0.39$; two-sided Wilcoxon sum-rank test) and no correlation between the degree of movement and response size (see Extended Data Figure 1 and Supplementary Information (SI) section 1). The spatial resolution of the OPM system was better than that of the cryogenic system, even with only 13 sensors (see Extended Data Figure 2 and SI section 2). These data, along with a similar analysis of evoked responses (see Extended Data Figure 3 and SI section 3), show clearly that the wearable system can be used to collect high fidelity data even in the presence of large head movements.

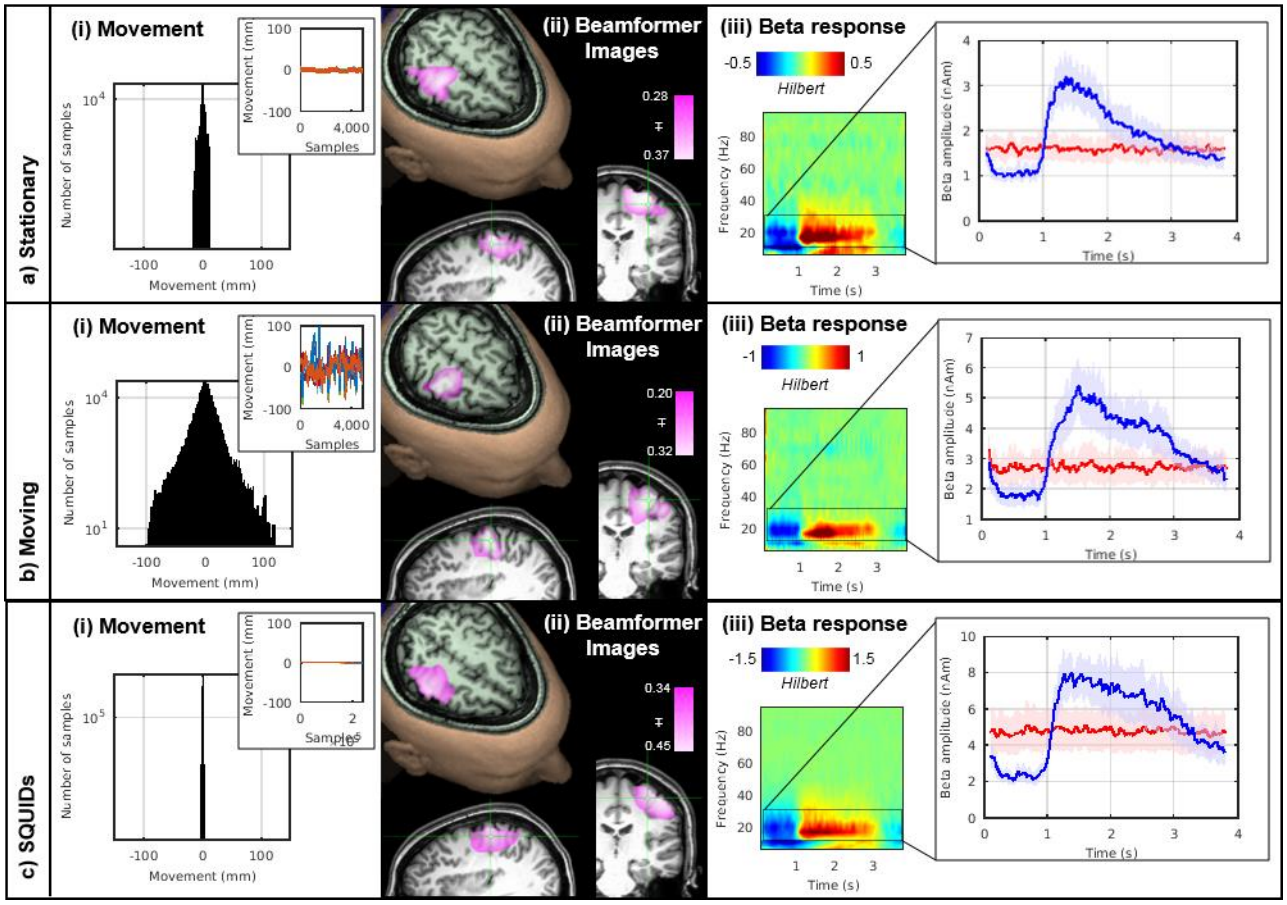

Figure 2: OPM-MEG results. *a) Shows the case when the subject was asked to remain still, b) shows the case when the subject was moving. c) Shows the case for data collected using a cryogenic MEG instrument for comparison. In (a), (b) and (c): i) A histogram showing movement of 3 fiducial markers on the subject's head. The inset graph shows the change in marker positions over a typical experiment; different colours show movement in 3 Cartesian axes of the three markers. ii) The change in beta band power due to finger abduction (purple) overlaid onto on axial, sagittal and coronal slices of the anatomical MRI – the functionally active region overlays contra-lateral sensorimotor cortex. iii) A time-frequency spectrogram depicting changes in neural oscillations during finger abduction. The inset graph shows the characteristic beta band response for finger abduction (blue) and rest trials (red). In all cases the results are averaged over trials and experiments and the shaded region shows standard error over 6 experiments. SIR ranged from 4.3 to 8.2 for static OPM measures, 4.2 to 5.8 for moving OPMs, and 4.9-7.9 for the cryogenic system. Further analysis (see extended data Figure 2 and SI section 2) showed that the OPM system significantly outperformed the cryogenic system in terms of both spatial resolution, and robustness across experiments. Temporal resolution was quantified at 130 Hz.*

Critical to the wearable MEG system is a means to null the background static magnetic field impinging on the OPMs. The system is housed inside a magnetically shielded room (MSR). However, the remnant earth's field in the MSR is ~25 nT, and spatially inhomogeneous. Any sensor movement through this field during a MEG recording would result in a field change much larger than the fields of interest, and would exceed the OPM's narrow (±1.5 nT) operational range, rendering them inoperable. In addition, such changes can modulate the sensor gain (see Extended Data Figure 4 and SI section 4). To ameliorate this problem, we constructed a set of bi-planar electromagnetic coils designed to generate fields equal and opposite to the remnant earth's field, thereby cancelling it out.

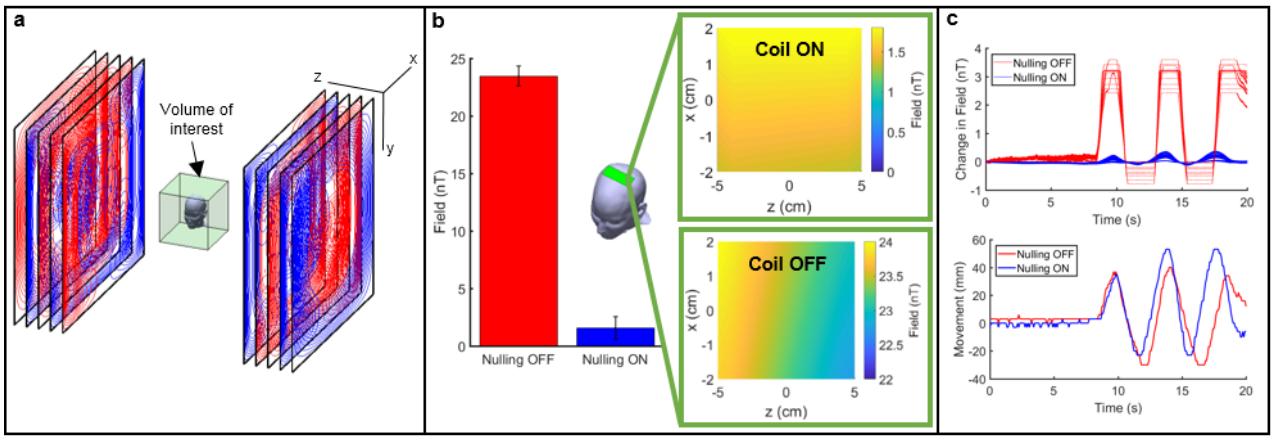

Figure 3: Bi-planar fingerprint-coil system for removing remnant static magnetic fields. *a) Schematic of the coils, which are confined to two planes surrounding a 40 x 40 x 40 cm^3 region of interest in which the head is allowed to move. The 5 separate layers represent wire paths that generate fields B_x, B_y, B_z, $^{dB_x}/_{dz}$ and $^{dB_z}/_{dz}$. b) Bar chart showing field magnitude with and without the field-nulling. Inset images show spatial field variation of B_x. The static field was reduced from 22±1 nT to 440±150 pT. $^{dB_x}/_{dz}$ measured across a 10 cm region spanning the width of the head (see the green box in b) was reduced from 10 nT/m to 0.28 nT/m. c) The upper plot shows the output of one OPM over time whilst the subject nods their head (head movement shown in lower plot). Blue and red traces show the cases where the field-nulling system was on and off, respectively. Note that without field nulling the OPMs saturate during head-movement whereas with nulling the sensors continue to work, leaving an artifact which is comparable in magnitude to that due to an eye-blink.*

The coils were designed[25,26] on two 1.6 x 1.6 m^2 planes, placed either side of the subject with a 1.5 m separation (Figure 3a). Three coils generated spatially uniform fields (B_x, B_y and B_z) whilst two additional coils were used to remove the dominant field variations ($^{dB_x}/_{dz}$ and $^{dB_z}/_{dz}$). In this way, unlike standard field-nulling technologies (e.g. tri-axial Helmholtz coils), our system is able to

account for spatial variation of the field over a 40 x 40 x 40 cm^3 volume of interest enclosing the head. Further, we were able to cancel all components of the field vector using coils confined to just two planes, hence retaining easy access to the subject. Four reference OPM sensors were coupled to the coils in a feedback loop to null the residual static field in the volume of interest. We achieved a 50-fold reduction in the remnant earth's field, and a 35-fold reduction in the dominant field gradient (Figure 3b). Figure 3c shows OPM measurements made during 7 cm head movements, with (blue) and without (red) field-nulling. The results show that without field-nulling the OPM sensors fail (evidenced by the saturation). With field nulling, however, the OPMs are able to capture MEG data even with the head moving (see also SI section 5).

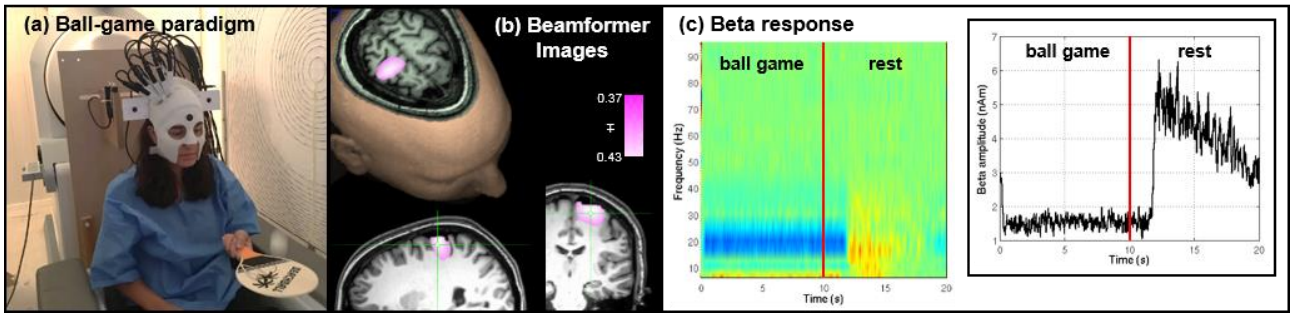

Figure 4: An example 'real world' imaging paradigm. *a) Experimental setup: the seated subject continually bounced a table tennis ball off a bat for 10 s; this was followed by a 10 s baseline period, in which they did nothing. This was repeated 29 times. b) Spatial signature of beta band oscillatory change during periods of playing the ball game compared to rest. Note the difference in localisation compared to Fig. 2, with the beta modulation localised to the arm/wrist area of sensorimotor cortex (distinct from the hand area in Fig. 2). c) Trial averaged time-frequency spectrogram and (inset) amplitude of beta oscillations averaged over time. The maximum head movement during this paradigm, assessed by the Kinect camera, was 6cm. This simple example demonstrates the power of wearable neuroimaging to accurately assess brain function during a real world visuo-motor coordination task. This example could readily be extended to examine e.g. the neural correlates of motor coordination, their maturation during neurodevelopment and their breakdown in movement disorders. Such studies using naturalistic stimuli are inaccessible to conventional neuroimaging scanners due to the movement required to undertake the task. To show robustness of this measure, similar data were captured in 2 further subjects. Task induced beta modulation, relative to baseline, was measured at X% X% and X% in the three participants.*

The ability to map human electrophysiology non-invasively, with whole brain coverage and high spatiotemporal resolution is unique to MEG[27]. Competitor techniques either lack spatial specificity (e.g. EEG – which is also more susceptible to muscle artifact, see Extended Data Figure 5 and SI

Section 6) or only provide indirect access to brain function via metabolic processes (e.g. fMRI). However, current MEG systems exclude many subject cohorts and experimental paradigms. Our system represents a step change for functional imaging. A wearable instrument with scalp-mounted sensors means that subjects can be scanned across the lifespan, from babies to elderly patients, allowing imaging during key stages of cognitive development and decline. For example, it is well known that efficient communication between spatially separate cortical regions is key to healthy brain function, and that neural oscillations help mediate such connectivity[28,29]. However, little is known about how electrophysiological brain networks emerge in the early years of life. Our system can characterise those networks, and the spectro-temporal profile of the connectivities that underlie them (see Extended Data Figure 6 and SI section 7). This highlights the potential utility of OPM-MEG for characterising the developmental connectome. Our wearable system also opens doors to myriad neuroscientific investigations in which subjects can move naturally and interact with the real world. An example is given in Figure 4 which shows brain activity elicited when the subject played a ball game (Figure 4a). This naturalistic paradigm requires free, rapid and unpredictable head and arm movement; nevertheless we were able to localise changes in beta oscillations to the arm/wrist area of motor cortex (Figure 4b) and track the dynamics of oscillatory modulation (Figure 4c). This shows the unique potential of wearable MEG to assess visuomotor coordination, adding a new dimension to previous work[30]. In sum, this new technology has transformative potential across a range of neuroscientific and clinical applications, where knowledge of brain electrophysiology is informative.

References:

1 Cohen, D. Magnetoencephalography: Detection of the brains electrical activity with a superconducting magnetometer. *Science* **5**, 664 - 666 (1972).

2 Kominis, I. K., Kornack, T. W., Allred, J. C. & Romalis, M. V. A subfemtotesla multichannel atomic magnetometer. *Nature* **422**, 596-599 (2003).

3 Shah, V. K. & Wakai, R. T. A compact, high performance atomic magnetometer for biomedical applications. *Physics in Medicine and Biology* **58**, 8153-8161. (2013).

4 Hamalainen, M. S., Hari, R., Ilmoniemi, R. J., Knuutila, J. & Lounasma, O. V. Magnetoencephalography: Theory, instrumentation, and applications to non-invasive studies of the working human brain. *Reviews of Modern Physics* **65**, 413-497 (1993).

5 Gross, J. *et al.* Good practice for conducting and reporting MEG research. *NeuroImage* **65** 349-363 (2013).

6 Allred, J., Lyman, R., Kornack, T. & Romalis, M. V. High-sensitivity atomic magnetometer unaffected by spin-exchange relaxation. *Physical Review Letters* **89**, Article Number: 130801 (2002).

7 Shah, V., Knappe, S., Schwindt, P. D. & Kitching, J. Subpicotesla atomic magnetometry with a microfabricated vapour cell. *Nature Photonics* **1**, 649-652 (2007).

8 Dupont-Roc, J., Haroche, S. & Cohen-Tannoudji, C. Detection of very weak magnetic fields (10-9 gauss) by 87Rb zero-field level crossing resonances. *Physics Letters A* **28**, 638-639 (1969).

9 Borna, A. *et al.* A 20-Channel Magnetoencephalography System Based on Optically Pumped Magnetometers. *https://arxiv.org/ftp/arxiv/papers/1706/1706.06158.pdf* (2017).

10 Alem, O., Benison, A. M., Barth, D. S., Kitching, J. & Knappe, S. Magnetoencephalography of Epilepsy with a Microfabricated Atomic Magnetrode. *Journal of Neuroscience* **34**, 14324-14327 (2014).

11 Alem, O. *et al.* Magnetic field imaging with microfabricated optically-pumped magnetometers. *Optical Express* **25**, 7849-7858 (2017).

12 Boto, E. *et al.* A new generation of magnetoencephalography: Room temperature measurements using optically-pumped magnetometers. *Neuroimage* **149**, 404-414 (2017).

13 Johnson, C., Schwindt, P. D. D. & Weisend, M. Magnetoencephalography with a two-color pump-probe, fiber-coupled atomic magnetometer *Applied Physics Letters* **97** (2010).

14 Johnson, C. N., Schwindt, P. D. & Weisend, M. Multi-sensor magnetoencephalography with atomic magnetometers. *Physics in Medicine & Biology* **58**, 6065-6077 (2013).

15 Kamada, K. *et al.* Human magnetoencephalogram measurements using newly developed compact module of high-sensitivity atomic magnetometer. *Japanese Journal of Applied Physics* **54**, Article number 026601 (2015).

16 Kiwoong, K. *et al.* Multi-channel atomic magnetometer for magnetoencephalography: A configuration study. *NeuroImage* **89** (2014).

17 Pfurtscheller, G. & Lopes da Silva, F. Event-related EEG/MEG synchronization and desynchronization: Basic principles. *Clin Neurophysio* **110**, 1842-1857 (1999).

18 Gaetz, W., Macdonald, M., Cheyne, D. & Snead, O. Neuromagnetic imaging of movement-related cortical oscillations in children and adults: Age predicts post-movement beta rebound. *Neuroimage* **51**, 792-807 (2010).

19 Mary, A. *et al.* Aging reduces experienceinduced sensorimotor plasticity. A magnetoencephalographic study. *NeuroImage* **104**, 59-68 (2015).

20 Robson, S. E. *et al.* Abnormal visuomotor processing in schizophrenia. *NeuroImage Clinical* **12**, 869-878 (2016).

21 Uhlhaas, P. J. & Singer, W. Abnormal neural oscillations and synchrony in schizophrenia. *Nature Reviews Neuroscience* **11**, 100-113 (2010).

22 Barratt, E. L. *et al.* Abnormal task driven neural oscillations in multiple sclerosis: A visuomotor MEG study. *Human Brain Mapping* **38**, 2441-2453 (2017).

23 Brookes, M. J. *et al.* Optimising experimental design for MEG beamformer imaging *NeuroImage* **39**, 1788-1802 (2008).

24 Van Veen, B. D., Van Drongelen, W., Yuchtman, M. & Suzuki, A. Localisation of brain electrical activity via linearly constrained minimum variance spatial filtering. *IEEE Transactions on biomedical engineering* **44**, 867-880 (1997).

25 Poole, M. & Bowtell, R. Novel gradient coils designed using a boundary element method. *Concepts in Magnetic Resonance Part B: Magnetic Resonance Engineering* **31**, 162-175 (2007).

26 Carlson, J. W., Derby, K. A., Hawryszko, K. C. & Weideman, M. Design and evaluation of shielded gradient coils. *Magnetic Resonance in Medicine* **26**, 4349-4353 (1992).

27 Baillet, S. Magnetoencephalography for brain electrophysiology and imaging. *Nature Neuroscience* **20**, 327–339 (2017).

28 Brookes, M. J. *et al.* Investigating the Electrophysiological Basis of Resting State Networks using Magnetoencephalography. *Proceedings of the National Academy of Science USA* **108**, 16783-16788 (2011).

29 Hipp, J. F., Hawellek, D. J., Corbetta, M., Siegel, M. & Engel, A. K. Large-scale cortical correlation structure of spontaneous oscillatory activity. *Nature Neuroscience* **15**, 884-890 (2012).

30 Jerbi, K. *et al.* Coherent neural representation of hand speed in humans revealed by MEG imaging. **104** 7676-7681 (2007).

MATERIALS AND METHODS

1) OPM-MEG SYSTEM DESIGN AND FABRICATION

1.1) System overview

An overview of our OPM-MEG system is shown in Extended Data Figure 7a. The system comprised 13 OPM sensors (QuSpin, Louisville, CO), which were mounted on the scalp surface (*the scalp array*), and a further 4 sensors (placed close to the head, but not on the scalp surface) which were used to make reference measurements (*the reference array*). Each sensor produces an analogue voltage output which is proportional to the magnetic field perpendicular to the laser beam (scaling = 2.7 V/nT). The sensor outputs were digitised at a sample rate of 1000 Hz, using a 16-bit digital acquisition (DAQ) system (National Instruments, Austin, TX) controlled using custom-written software in LabVIEW. The sensor arrays were housed inside a magnetically shielded room (MSR) to reduce environmental magnetic interference; all control equipment was kept outside the room to minimise its effect on MEG measurements.

Prior to data acquisition, the reference array was used to identify the currents in the coils which best nulled the residual static magnetic field inside the MSR and its dominant first order spatial variation. Reference sensors were located and oriented such that the three Cartesian components of the magnetic field (B_x, B_y and B_z), and the two dominant field gradients ($^{dB_x}/_{dz}$ and $^{dB_z}/_{dz}$) could be measured close to the head (see Extended Data Figure 7b). Reference array measurements were input to a proportional integral derivative (PID) algorithm, which was used to control the currents in the field-nulling coils. This allows the calculation of currents which generate fields that are equal and opposite to those measured by the reference array, thus attenuating the static field over the volume spanning the subject's head. This step is key if the head is free to move during MEG data acquisition, since without field-nulling, even small changes in head position or orientation (e.g. a 4° rotation in a 25 nT field) would produce field variations large enough to render the OPMs inoperable (see Figure 3c).

During data acquisition, all 17 sensors (13 sensor scalp array and 4 sensor reference array) were operated simultaneously, with the reference sensors (which are sufficiently far from the scalp to be insensitive to the neuromagnetic field) used to characterise temporally varying background magnetic interference, which was later regressed from the signals recorded by the scalp-mounted sensors.

The visual cue for paradigm control was controlled by a separate stimulus computer. This was coupled to a data projector which projected the cue image through a waveguide onto a back-projection

screen positioned ~40 cm in front of the subject. The stimulus computer also generated TTL trigger pulses of 1 s duration denoting the onset of the visual cues and the start of the rest periods. These trigger signals were input to the DAQ and sampled, simultaneously with the OPM data, at 1000 Hz. Throughout data acquisition, an Xbox Kinect camera (Microsoft, Redmond, WA) was used to measure head movement. Video data were captured using a third computer, which also recorded the trigger channels so that movement data could be later analysed on a trial-by-trial basis.

1.2) OPM sensors

The fundamental building block of our system is the OPM sensor. We employed compact commercially available sensors (see Figure 1c)[3,11], allowing a large number to be located flexibly on the scalp surface. Each OPM sensor head contains a semiconductor laser for optical pumping, optics for laser beam conditioning, a 3 x 3 x 3 mm^3 ^{87}Rb vapour cell and a silicon photodiode for beam detection. The sensor head connects to a small electronics controller via a 5 m cable which is passed through a waveguide in the MSR. The sensor includes three on-board coils which can be used to null static field components in the cell. Field changes (e.g. due to neural currents in the brain) can be detected via the change in transmitted light intensity which they produce (Figure 1b). The transmitted intensity shows a zero-field resonance, which is a Lorentzian function of the magnetic field components transverse to the laser beam, with a full width at half maximum of around 30 nT. For continuous field measurements, a sinusoidally-modulated magnetic field of 1 kHz frequency is applied perpendicular to the laser beam using the on-sensor coils. The depth of modulation of the transmitted light, which is monitored using a lock-in process, is sensitive to the magnitude of the field component along the modulation axis[8,31]. The amplitude of the two field components perpendicular to the beam can be measured simultaneously by applying oscillating currents to two coils in quadrature. However, here only the radial field component was measured.

1.3) Scanner-cast design and 3D printing

Pre-recorded MRI and (cryogenic) MEG data were used to inform the design and construction of the individualised scanner-cast. To ascertain the shape of the subject's head, an anatomical MRI scan was acquired using a Philips (Best, NL) 3T Ingenia MR system running a T1-weighted gradient echo imaging sequence, with an isotropic resolution of 1 mm and a high bandwidth to limit field-inhomogeneity-related distortion. A 3D mesh, representing the outer surface of the head and face was extracted from this image and then used to define a custom-fitted helmet, in which the OPM sensors could be mounted[12]. In a complete system, a large number of sensors would be spaced equidistantly across the entire scalp surface, giving whole brain coverage, but in our prototype system (used for the finger abduction and ball game paradigms), only 13 sensors were available and these had to be

positioned for optimal coverage of the sensorimotor region. To determine the optimal OPM sensor positions, we carried out the visually-cued finger abduction experiment on the same subject using a cryogenic MEG system, and localised the source position and orientation using a beamformer. Having computed the location and orientation of the dipolar source, we used a forward model to compute the radial magnetic fields at the scalp surface generated by this dipole. The positions of the scalp-array sensors were then chosen to sample these fields optimally[12]. We assessed the effect of crosstalk between sensors, which may occur due to constructive interference of fields from adjacent sensors. For the sensor array used here we found these effects to be less than 3% when taking into account the radial field (see Extended Data Figure 8 and SI section 8). See SI Section 7 for details of the scanner-cast that accommodated the 26 sensors which were used in a functional connectivity demonstration (see also Extended Data Figure 6).

1.4) Field Nulling Coils

The remnant earth's field at the centre of our MSR is ~25 nT, and also shows significant spatial variation, with a gradient of ~10 nTm^{-1}. This means that translation through the inhomogeneous remnant field, or rotation with respect to the field vector, produces field changes at the sensors that are much larger than the neuromagnetic fields of interest (as shown in Figure 3). Given the size of the remnant field and the narrow operational range of the OPMs (±1.5nT), such movement is likely to take the sensors outside their operational range. For example, a rotation of less than 4^o in a field of 25 nT can produce a change of more than 1.5 nT in the amplitude of the magnetic field along an OPM sensor's sensitive axis, thus rendering it inoperable. The use of the field nulling coils to reduce the remnant static (earth's) field over a large central volume inside the MSR is therefore critical if the sensor array is to be operated without being rigidly fixed in position with respect to the MSR.

Here, the remnant field was nulled using a set of coils positioned on either side of the subject (see Figure 3a). Five different bi-planar coils were constructed independently to null B_x, B_y and B_z and the two dominant field gradients, dB_x/dz and dB_z/dz. In contrast to the tri-axial Helmholtz coil arrangement that is commonly used to null the remnant field inside an MSR, the bi-planar coil array allows cancellation of spatially varying fields and also does not significantly limit access to the subject, since the coil windings are confined to two vertical planes (rather than the three pairs of orthogonal planes that would enclose the subject when using three orthogonal Helmholtz coils). The bi-planar coil system therefore offers significant advantages by eliminating the spatially uniform remnant field and its first order spatial variation, whilst maintaining access to the subject.

Magnetic fields from bi-planar coils[32] were optimised for homogeneity using a harmonic minimisation approach[26]. The current distribution $\boldsymbol{J}$ was confined to the two planes at $z = \pm a$ in the region $|x|,|y| < L$, and defined using the stream function, S as $\boldsymbol{J} = \nabla S \times \hat{\boldsymbol{z}}$. S is parameterised as a two-dimensional Fourier series so that

$$S = \sum_n \left[\alpha_n \frac{\cos\left(n-\frac{1}{2}\right)\pi x}{L} + \beta_n \sin\frac{n\pi y}{L} \right] \times \sum_m \left[\gamma_m \frac{\cos\left(m-\frac{1}{2}\right)\pi x}{L} + \delta_m \sin\frac{m\pi y}{L} \right]. \quad [1]$$

Optimal values of the Fourier coefficients (α_n , β_n, γ_m , δ_m) were identified by exploiting the symmetry of the field distribution and then minimising:

$$\sum_t \left[\boldsymbol{B}(\boldsymbol{r}_t) - \boldsymbol{B}_{target}(\boldsymbol{r}_t) \right]^2 + \omega P, \quad [2]$$

where $\boldsymbol{r}_t$ characterise locations within the volume of interest at which a homogenous field or field gradient (described by $\boldsymbol{B}_{target}$) is required, and P represents the power dissipated in the coil. The coefficient, ω can be used to adjust the weighting of the power term. Increasing ω reduces the complexity of the wire paths to be fabricated. $\boldsymbol{B}(\boldsymbol{r}_t)$ was calculated using the relationship

$$\widetilde{\boldsymbol{B}} = \mu_0 \left\{ \left[ik_x \hat{\boldsymbol{x}} + ik_y \hat{\boldsymbol{y}} \right] \begin{matrix} sinh \\ cosh \end{matrix} (k_r z) - k_r \hat{\boldsymbol{z}} \begin{matrix} cosh \\ sinh \end{matrix} (k_r z) \right\} \tilde{S} e^{-k_r a}, \quad [3]$$

where $\widetilde{\boldsymbol{B}}$ and $\tilde{S}$ are the two-dimensional Fourier transforms of the field and stream function with respect to x (k_x) and y (k_y), and $k_r = \left(k_x^2 + k_y^2\right)^{1/2}$. The upper/lower $sinh/cosh$ terms correspond to the case of the stream function having the same/opposite sign on the two planes. Coils were designed to produce a homogeneous (within ±5 %) field or field gradient over a 0.4 x 0.4 x 0.4 m^3 central region, which is large enough to span the range of sensor positions during experiments in which head movement is allowed. The wire paths for each coil span an area of 1.6 x 1.6 m^2 and are layered on two planes of medium-density fibreboard separated by 1.5 m. The coil wire paths and contours of the magnetic field or field gradient in a central plane between the two coils are shown in Extended Data Figure 9 for each coil. The field variation was calculated by applying the elemental Biot-Savart law to the digitised wirepaths (see SI section 5 for further discussion).

1.5) Motion detection and quantification

To quantify head movement, we used a simple optical tracking system based upon a Microsoft Kinect V1-2010 camera which was placed ~1 m in front of the subject. This camera provides a simultaneous 8-bit RGB video stream (640 x 480 pixel display, with 57° horizontal and 43° vertical field of view) and an 11-bit depth image, reconstructed from an infra-red projected field. Data from both streams were captured using the MATLAB image acquisition toolbox, at 12 frames per second.

A motion-tracking algorithm was used to track the positions of three black dots on the outer surface of the white scanner-cast. The algorithm was initiated via manual selection of the three dots in the first frame of the video. A threshold detect routine then identified the dots and their centre of mass in all subsequent frames. Pixel numbers were converted to absolute locations in three dimensions by integrating the video data with the depth field. In this way, we defined parameters describing the motion of the three markers throughout the experiment. To quantify motion, movement parameters for all three orientations and all three fiducial locations were concatenated. Figure 2 (panel i) shows these data as a histogram plotted on a logarithmic scale.

2) EXPERIMENTAL METHOD

2.1) Finger abduction paradigm

Experiments were carried out on a single subject (female, right-handed, age 27), who provided written informed consent (both to participation in the experiments and to release of photographs). The study was approved by the University of Nottingham Medical School ethics committee. The subject undertook multiple repeats of a visuo-motor task[20]. The paradigm comprised visual stimulation with a centrally-presented, maximum-contrast, vertical square-wave grating (3 cycles per degree). The grating subtended a visual angle of 8° and was displayed along with a fixation cross on a grey background. In a single trial, the grating was presented for 1 s followed by a 3 s baseline period during which only the fixation cross was shown. During presentation, the participant was instructed to make repeated abductions of their left (non-dominant) index finger. 50 of these trials were recorded in each experiment. Blocks of ten trials were interspersed with blocks of ten 'rest' trials. In these rest trials (also 4 s in duration) the fixation cross remained on the screen, but no finger abduction was made. Averaging across the 50 'real' and 50 'rest' trials independently allowed assessment of SIR (see below). This experiment was repeated six times with the subject stationary and six times with the subject making natural movements. It was also repeated six times using a cryogenic MEG system.

2.2) The 'ball game' paradigm

The subject was seated in the OPM-MEG system and asked to play a simple ball game in which they continually bounced a table tennis ball on a bat. 10 s bursts of 'ping-pong' were interspersed with 10 s of baseline activity (during which the subject was told to simply hold the bat and ball on their knee). This gave a total trial length of 20 s, and the subject repeated this 29 times. Due to the location of the OPM sensors in the scanner cast, the experiment was undertaken with the subject's non-dominant hand. Trials were cued by a second experimenter who was positioned inside the MSR throughout the experiment and gave verbal instructions to cue the game (they shouted either 'ping-pong' or 'rest' to

begin or stop the game). This experiment was undertaken once in the OPM-MEG system by three subjects.

2.3) Cryogenic MEG system data acquisition

To compare OPM-MEG to cryogenic-MEG recordings, we undertook the finger abduction experiment, in the same subject, using a 275-channel CTF MEG system (MISL, Coquitlam, Canada) operating in third-order synthetic gradiometer configuration[33]. Data were acquired at a sampling frequency of 600 Hz and the subject was seated. Three electromagnetic position indicator coils were placed on the head as fiducial markers (at the nasion, left preauricular and right preauricular points). The locations of these fiducials were tracked continuously during the recording by sequentially energising each coil and performing a magnetic dipole fit to these data. This allowed both continuous assessment of head movement throughout the measurement, and knowledge of the location of the head relative to the MEG sensors. Prior to the MEG recording, a 3-dimensional digitisation of the subject's head-shape, relative to the fiducial markers, was acquired using a 3D digitiser (Polhemus Inc., Vermont). Co-registration of the MEG sensor geometry to the anatomical MR image was achieved by fitting the digitised head surface to the equivalent head surface extracted from the anatomical image. The subject undertook the experiment six times and a different head digitisation was acquired each time.

2.4) Data processing: interference rejection

Following data collection, OPM-MEG data were processed in order to remove magnetic interference. The reference array sensors were located close enough to the scalp array to capture similar environmental interference, but sufficiently far away to be insensitive to the neuromagnetic fields of interest. This meant that the scalp and reference arrays could be used to synthesise a 'gradiometer' measurement whereby the scalp array data are de-noised via regression of the reference array signals[12]. The reference array data from all four channels were combined in a single (design) matrix and a regression was used to remove any linear combination of reference array (interference) signals from the scalp array (neuromagnetic) signals. We applied this correction to the raw (i.e. unfiltered) data.

2.5) Data processing: beamforming

Following interference rejection, all MEG data (OPM and cryogenic) were processed in the same way. Data were initially inspected visually, and any trials with excessive interference were discarded. This resulted in the loss of only 1 trial (from a cryogenic recording). A beamformer adaptive spatial filtering approach was then employed.

Using a beamformer[24,34], an estimate of electrical source strength $\hat{Q}_{\boldsymbol{\theta}}(t)$, made at time *t* and a predetermined location in the brain is given by a weighted sum of sensor measurements such that

$$\hat{Q}_{\boldsymbol{\theta}}(t) = \mathbf{W}_{\boldsymbol{\theta}}^{T}\mathbf{m}(t). \qquad [4]$$

Here $\boldsymbol{m}(t)$ is a vector of magnetic field measurements made at time *t* across all sensors (i.e. 13 in our OPM system or 275 in the cryogenic system) and $\mathbf{W}_{\boldsymbol{\theta}}$ is a vector of weighting parameters tuned to a predefined location in source-space and current dipole orientation, represented by the vector $\boldsymbol{\theta}$. The superscript *T* indicates a matrix transpose.

The weighting parameters are derived based on power minimisation. The overall power in the output signal $\hat{Q}_{\boldsymbol{\theta}}(t)$ is minimised with the linear constraint that power originating from the location/orientation of interest ($\boldsymbol{\theta}$) should remain. Mathematically the beamformer problem can be written as:

$$\min_{\mathbf{W}_{\boldsymbol{\theta}}}\left[\hat{Q}_{\boldsymbol{\theta}}^{2}\right] \quad \textit{subject to} \quad \mathbf{W}_{\boldsymbol{\theta}}^{T}\mathbf{L}_{\boldsymbol{\theta}} = 1, \qquad [5]$$

where $\hat{Q}_{\boldsymbol{\theta}}^{2}$ represents the source power, given by $\hat{Q}_{\boldsymbol{\theta}}^{2} = \mathbf{W}_{\boldsymbol{\theta}}^{T}\mathbf{C}\mathbf{W}_{\boldsymbol{\theta}}$, $\mathbf{C}$ represents the channel level data covariance matrix calculated over a time-frequency window of interest, and $\mathbf{L}_{\boldsymbol{\theta}}$ is the lead field vector, which is a vector containing a model of the magnetic fields that would be measured at each of the sensors in response to a source of unit amplitude with location and orientation $\boldsymbol{\theta}$. The (regularised) solution to Eq. 5 is found analytically to be:

$$\mathbf{W}_{\theta}^{T} = \left[\mathbf{L}_{\theta}^{T}\{\mathbf{C}+\mu\boldsymbol{\Sigma}\}^{-1}\mathbf{L}_{\theta}\right]^{-1}\mathbf{L}_{\theta}^{T}\{\mathbf{C}+\mu\boldsymbol{\Sigma}\}^{-1} \quad . \qquad [6]$$

$\boldsymbol{\Sigma}$ is a diagonal matrix representing the white noise at each of the MEG channels (which we approximate as the identity matrix) and μ is a regularisation parameter[35]. Note that, in addition to source localisation, the power minimisation term has the desirable effect of reducing artifact from e.g. muscles (see Extended Data Figure 10 and SI section 9).

We sought to examine beta band effects, and so the beamformer weights were constructed, using Eq. 6, with covariance matrix $\mathbf{C}$ computed using beta band (13-30 Hz) data over a time window spanning the entire experiment[23] (400s). In all cases (OPM and cryogenic MEG data) the regularisation parameter was optimised to give the best SIR (defined as the standard deviation of the finger abduction trials divided by the standard deviation of the rest trials). The lead field was calculated using the analytical formulation first described by Sarvas[36]. Two other covariance matrices were constructed: $\mathbf{C}_{a}$ was defined as the data covariance in an 'active' window. This spanned the 0 s < t

< 1 s window (relative to trial onset) in the case of the finger abduction paradigm, and the 1 s < t < 9 s window (relative to trial onset) in the ball game paradigm. $\mathbf{C}_c$ represented data covariance in a 'control' window (1 s < t < 2 s for the finger abduction and 11 s < t < 19 s for the ball game). We then defined a pseudo-T-statistical contrast as

$$T = \frac{\mathbf{W}_\theta^T \mathbf{C}_a \mathbf{W}_\theta - \mathbf{W}_\theta^T \mathbf{C}_c \mathbf{W}_\theta}{2\mathbf{W}_\theta^T \mathbf{C}_c \mathbf{W}_\theta} \quad [7]$$

Pseudo-T-statistics were computed at the vertices of a regular 4 mm grid spanning the entire brain. For each voxel, the orientation of each source was based on a non-linear search for the orientation that gave the maximum signal to noise ratio[34]. This method allowed construction of 3D images showing the spatial signature of maximum change in beta power. These images, averaged across experiments, are shown in Figure 2 (panel ii) and in Figure 4b.

Finally, to investigate the spectro-temporal signature of electrophysiological activity at the location of peak change, a time-frequency spectrogram (TFS) was derived. Here, the peak location/orientation, θ_{peak}, was extracted from the beamformer images, and a time course of electrophysiological activity for that location derived using Eq. 4 (the data covariance for the weights calculation was expanded to a broad (1-150 Hz) frequency range and covered the full 400s of data collection). The resulting data were frequency filtered into 31 overlapping frequency bands, and a Hilbert transform was used to generate the amplitude envelope of oscillations within each band. These envelope time courses were then averaged across trials, and experiments, and concatenated in the frequency dimension to generate a single TFS (shown in Figure 2, panel iii, and in Figure 4c). The same method was used (with beta band filtered covariance for weights calculation) to examine beta band fluctuations.

31 Shah, V., Knappe, S., Schwindt, P. D. D. & Kitching, J. Subpicotesla atomic magnetometry with a microfabricated vapour cell. *Nature Photonics* **1**, 649-652 (2007).

32 Yoda, K. Analytical design method of shelf shielded planar coils. *Journal of Applied Physics* **67**, 191-206 (1990).

33 Vrba, J. & Robinson, S. E. Signal processing in magnetoencephalography. *Methods* **25** (2001).

34 Robinson, S. & Vrba, J. Functional Neuroimaging by synthetic Aperture Magnetometry. *In Recent Advances in Biomagnetism, ed. Yoshimoto T, Kotani M, Kuriki S, Karibe H, Nakasato N, Tohoku Univ. Press, Sendai, Japan.*, 302-305 (1998).

35 Backus, G. E. & Gilbert, F. The Resolving power of Gross Earth Data. *Geophysical Journal of the Royal Astronomical Society* **16**, 169-205 (1968).

36 Sarvas, J. Basic mathematical and electromagnetic concepts of the biomagnetic inverse problem. *Physics in Medicine and Biology* **32**, 11 - 22 (1987).

Acknowledgements

This study was funded by a Wellcome Collaborative Award in Science (203257/Z/16/Z and 203257/B/16/Z) awarded to GRB, RB and MJB. We also acknowledge the UK Quantum Technology Hub for Sensors and Metrology, funded by the Engineering and Physical Sciences Research Council (EP/M013294/1). We acknowledge Medical Research Council Grants (MR/K005464/1 and MR/M006301/1). The Wellcome Centre for Human Neuroimaging is supported by core funding from Wellcome [203147/Z/16/Z]. OPM sensor development at QuSpin was supported by National Institutes of Health grants R44HD074495 and R44MH110288. The scanner casts were designed and manufactured by Mark Lim at Chalk Studios Ltd.

Supplementary Information

3) TRIAL-BY-TRIAL ANALYSIS

We present an additional analysis of the data from the 6 finger-abduction experiments, where the subject was asked to make naturalistic movements of their head during data acquisition. Here, data from the Xbox Kinect camera and OPM MEG channels were combined to examine the effect of subject movement on beta band response magnitude, on a trial-by-trial basis. Initially, all data (movement, trigger, and OPM-MEG) were concatenated across all six experiments. Kinect data were divided into trials and the maximum movement within every trial computed as the largest difference between measured fiducial marker coordinates (we took the maximum movement of the three different fiducials in any of the three Cartesian axes). For each trial, the mean beta amplitude during the window containing the power-decrease ($0.4 < t < 0.9$ s), and the rebound (1.05 s $< t < 4.0$ s) was also computed. The difference between these two metrics was taken as the peak-to-peak response magnitude. We then tested for any significant correlation between response magnitude and movement.

Extended Data Figure 1a shows beta envelopes (for both the finger abduction and the rest trials) in the presence of large (50 % of trials with highest movement) and small (50 % of trials with smallest movement) motion. Here, the red trace shows the beta band amplitude in finger abduction trials in the presence of (on average) a 4.3 cm within-trial head movement; the blue trace shows a similar plot for data recorded in the presence of a 1.7 cm movement. The green and black traces show the case for resting trials with 4.4 cm and 1.7 cm movements, respectively. Interestingly, there was a significant increase in baseline beta band oscillatory amplitude for the larger head movement, in both the resting and finger abduction trials. This was thought to relate to an increase in artifact due to electrophysiological activity in the muscles in the neck. However, despite a more than doubling of the head movement, the actual beta response magnitude to finger abduction remains similar. To quantify this, Extended Data Figure 1b shows the measured peak-to-peak response amplitude plotted against motion for all trials. No measurable relationship between movement and beta response magnitude was observed, showing that data quality was unaffected by movement. (If data quality was degraded we would expect a negative relationship.)

4) SPATIOTEMPORAL RESOLUTION AND ORIENTATION ROBUSTNESS

To further characterise our OPM-MEG system we undertook three separate analyses of the finger abduction data, the first was to quantify spatial resolution, the second to better understand the scan-to-scan repeatability, and the third to assess temporal resolution.

Spatial resolution measurement

To compute spatial resolution we measured the correlation between two beamformer reconstructed timecourses as a function of the spatial separation between them[1]. A 'seed' location was selected in sensorimotor cortex (based upon the peak location of beta band response – this is denoted by the cross hair in Extended Data Figure 2a). 4000 'test' locations, within 3cm of the seed, were then selected randomly (marked as the red overlay in Extended Data Figure 2a). Data were filtered into the beta frequency band and the beamformer used to extract timecourses of electrophysiological activity (see Materials and Methods) for the seed and all test locations. Pearson correlation was measured between all seed-test pairs; correlation values were binned according to seed-test distance and averaged within each bin. (20 bins were used, spaced evenly between 0 and 3 cm meaning that 200 seed-test pairs were averaged for each bin.) In order to avoid confounds associated with source orientation, all reconstructed orientations were forced to be the same as that of the seed. To estimate spatial specificity of the system, we computed the average seed-test distance for which shared variance between reconstructed timecourses fell to <50 % - this metric serves as a quantification of spatial resolution. This measurement was made independently for 18 separate experiments – 6 OPM runs with no head movement, 6 OPM runs with head movement and 6 runs using the cryogenic MEG system. Spatial resolution was averaged for each experimental condition and we tested for differences between conditions using a non-parametric Wilcoxon sum-rank test.

Results of this analysis are shown in Extended Data Figure 2b. The line graph shows correlation between the seed and test timecourses plotted as a function of separation. The bar chart shows source separation for which shared variance dropped to <50 %. In both cases, results are shown for the three different experimental conditions and error bars show standard deviation over six experiments. The highest spatial resolution was achieved in the static OPM case. Spatial resolution dropped slightly (although not significantly ($p = 0.09$)) when the subject made naturalistic head movements. This is a consequence of the beamformer and is a well characterised effect[1] – briefly, the limited degrees of freedom in the MEG data mean that spatial resolution drops if the beamformer is forced to supress artifacts. Here, artifacts were generated by the muscles in the neck controlling head movement – in nulling these artifacts (see Extended Data Figure 10 and SI section 9), the spatial resolution would be expected to decrease slightly. Spatial resolution was lowest for the cryogenic system. The difference in spatial resolution between static OPMs and the cryogenic system was significant ($p = 0.002$). The difference between OPMs with movement and the cryogenic system was not significant ($p = 0.09$).

Scan-to-scan robustness

To assess scan-to-scan reliability we adopted a recently developed approach based upon the known origins of the MEG signal[2-4]. Source power can vary between experiments. However because the MEG signal is driven by current flow in pyramidal neurons, and pyramidal neurons are mostly oriented perpendicular to the cortical surface, source orientation depends only on the local folding of the cortical sheet. This means that source orientation should remain the same across two or more equivalent experiments (where the same sources are active). To test this in the present data, we again selected 4000 source locations within 3cm of the peak beta modulation in sensorimotor cortex. For each location, we computed source orientation independently for each of the 6 experiments. We then measured the orientation difference (as an angle) for all possible combinations of the 6 experiments (i.e. for any one source location, 6 experiments means 15 possible comparisons of source orientation; 4000 test locations thus meant 60,000 angle differences were calculated). We plotted these angles as a histogram, and we expected the histogram to peak at zero. These calculations were undertaken separately for each experimental condition. To assess the difference between conditions we computed the probability of an orientation discrepancy less than 5 degrees. To assess statistical significance a permutation test was employed. We undertook the same calculation but with orientation differences assigned randomly to 'sham' conditions. In this way a null distribution was constructed and an empirical p-value determined by comparing the real data to the null distribution. Significance was assigned based on $p < 0.05$, multiple comparison corrected using the Bonferroni Method.

Results are shown in Extended Data Figure 2c. The three histograms show the orientation difference for the static OPM (top) moving OPM (centre) and cryogenic (bottom) cases. In all three cases, as expected, the derived probability distribution peaks at zero showing the reproducibility of the measurements across experiments. The bar chart shows the probability of observing an angular discrepancy < 5 degrees. Here we see clearly that the OPM array, when static, significantly ($p < 0.05$) outperformed the cryogenic system in terms of orientation robustness. Moving OPMs demonstrated the lowest robustness, however this would be expected since the execution of natural movements differed across runs, and therefore the 6 experiments cannot be considered equivalent. This result, combined with the spatial resolution measurement above, shows that even with only 13 sensors, our OPM-MEG array outperforms a state of the art 275 channel cryogenic MEG system. These data therefore demonstrate the significant promise of future generations of OPM-MEG systems to vastly outperform current MEG technology.

Temporal resolution

Temporal resolution is limited by the bandwidth of the OPM sensors. Bandwidth itself is a function of the transverse spin relaxation rate of the alkali metal atoms, and hence represents a fundamental limitation of our system. To measure this experimentally, we constructed a small Helmholtz coil, with a coil radius and separation of 15 cm. A single OPM was placed with its sensitive volume at the centre of this Helmholtz coil, and a white noise signal was applied to the coil windings. The OPM output was measured over a 120 s period, and a comparison of the Fourier transformed input signal and OPM data used to compute the frequency at which the OPM sensitivity was significantly reduced (quantified as the 3 dB point). The result is shown in Extended Data Figure 2d: the blue line shows the spectrum of the current source, the green line shows the spectrum of the measured field. These data suggest that sensitivity decreases significantly above 130 Hz (a temporal resolution of 7.7 ms). It is noteworthy that this bandwidth is lower than that of superconducting quantum interference devices (SQUIDs), however it remains sufficiently high to capture most signals that are of interest in MEG.

5) EVOKED RESPONSE ANALYSIS

In addition to neural oscillatory responses, task-based MEG studies often seek to measure the time- and phase-locked evoked responses to stimuli; that is, the broad-band transient component of the electrophysiological response (in this case to finger-movement). This is somewhat complicated in the present work because movement onset depends on reaction time to the visual cue, and therefore differences in reaction time across trials will attenuate the average evoked response. Nevertheless we undertook an evoked analysis which employed similar beamformer techniques to those described in our methodology section.

Differences for this supplementary analysis were that the data were frequency filtered between 2 Hz and 30 Hz to best capture the evoked response. To attenuate low frequency artifacts, raw data at the OPM sensor level were treated on a trial-by-trial basis, with a 10^{th} order polynomial fitted to, and removed from, each trial (and each sensor). The beamformer was applied as described in our Methods section, with covariance ($\mathbf{C}$) computed using unaveraged data in the 2-30 Hz band and a time window spanning the entire set of six experiments. Pseudo-T-statistical images were generated using Eq. 7: $\mathbf{C}_a$ was defined as the covariance computed using the trial averaged data in an 'active' window spanning 0 s < t < 0.5 s relative to trial onset. $\mathbf{C}_c$ was defined using trial averaged data with the control window set to 1.5 s < t < 2 s. Electrophysiological time courses were extracted from the peak in the pseudo-T-statistical images, and averaged across both finger abduction and rest trials. The

signal to interference ratio (SIR) was computed as the ratio of the standard deviation of the average signal in the finger abduction trials (in the 0 s < t < 1 s window) to the equivalent standard deviation in the rest trials. SIR values were calculated for each of the 12 OPM experiments (6 static and 6 moving) independently.

Results are shown in Extended Data Figure 3, separately for the following experimental conditions: experiments where the subject was asked to make natural head movements whilst performing the finger abductions are shown in Figure 3b; experiments where the subject was asked to remain still are shown in Figure 3a. In both cases, panel (i) shows the beamformer image and the evoked response time courses. Extended Data Figure 3c shows a direct comparison of the evoked response to finger abduction for moving (blue) and static (red) data. Importantly, the spatio-temporal signature of the response in the two cases is largely similar. Quantitatively, for the static case, SIR ranged from 1.4 to 2.1, whilst for the moving case SNR ranged from 1.0 to 1.9; no significant difference was observed ($p = 0.24$; two-sided Wilcoxon sum-rank test). These results show once again that our system can capture high quality MEG data, even in the presence of large movements.

6) OPM CALIBRATION IN A CHANGING BACKGROUND FIELD

At any single point in time, the OPM cell can be thought of as experiencing two magnetic fields: one (time varying) field due to the brain, and a second (temporally invariant) field due to the background static (earth's) magnetic field. At the beginning of the experiment, the latter is reduced by the field nulling coils over a large volume through which the head can move. Although inevitably this cancellation is imperfect, it is sufficient to allow the sensors to remain operational in the presence of head movements, and to reduce the movement-related artifact to a manageable level (see Fig. 3). However, a more subtle effect is that changes in the background field also alter the gain of the OPM. Specifically, as the background field increases the gain of the sensor reduces and the OPM sensitivity to neuromagnetic fields drops. For the purposes of the present paper, it is critical that this effect is characterised, since significant variation in the gain across an experiment would degrade the accuracy of the beamformer spatial filter used to process the data.

The measured output of a single OPM channel (i.e. the output of the photodiode) is a Lorentzian function of the magnetic field inside the vapour cell. In practice, an oscillating field of frequency ω, oriented perpendicular to the laser beam, is added by on-board coils. This allows us to read out a signal proportional to the component of the time-varying field that is parallel to the modulation field. To illustrate this mathematically, assume that the laser beam is oriented along the *z*-axis, and the field of interest in the cell, B_x, is oriented in the x direction, as is the modulation field. In this case, the

output OPM signal (which is proportional to polarisation in the *z*-direction, $P_z(\omega)$) is given by a solution to the Bloch Equation[5,6]:

$$P_z(\omega) \propto \left(\frac{\gamma^2\tau^2 B_x}{\gamma^2\tau^2 B_x^2+1}\right) sin(\omega t) J_0\left(\frac{\gamma B_{mod}}{Q(P)\omega}\right) J_1\left(\frac{\gamma B_{mod}}{Q(P)\omega}\right). \quad [s1]$$

Here, γ is the electron gyromagnetic ratio and τ $(= R + \frac{1}{T_2})^{-1}$ is the atomic spin coherence time, which is a function of both the optical pumping rate, R, and the relaxation time T_2. J_0 and J_1 are Bessel functions of the first kind. B_{mod} is the modulation field amplitude and $Q(P)$ is the nuclear slow-down factor which depends on the spin polarisation. Assuming a lock-in process is used to measure the component of P_z varying at frequency ω then, since the product $J_0\left(\frac{\gamma B_{mod}}{Q(P)\omega}\right) J_1\left(\frac{\gamma B_{mod}}{Q(P)\omega}\right)$ is constant, we can write

$$P_z(\omega) \propto \left(\frac{\gamma^2\tau^2 B_x}{\gamma^2\tau^2 B_x^2+1}\right). \quad [s2]$$

Now assume that the field component of interest, B_x, comprises two parts: a static or background field, $B_x^{(static)}$, and a neuromagnetic field δB_x so that

$$B_x = B_x^{(static)} + \delta B_x \quad [s3]$$

Assuming that the remnant earth's field is larger than the neuromagnetic field (i.e. $B_x^{(static)} \gg \delta B_x$) then

$$P(\omega) \propto \left(\frac{\gamma^2\tau^2}{\gamma^2\tau^2 B_x^{(static)2}+1}\right) B_x^{(static)} + \left(\frac{\gamma^2\tau^2}{\gamma^2\tau^2 B_x^{(static)2}+1}\right) \delta B_x. \quad [s4]$$

Here, the first term relates to the sensor response to the changing static field (i.e. the movement artifact) and the second term corresponds to the sensor response to neuromagnetic field changes. Importantly, the effective gain of the output due to the neuromagnetic field, which can be written as

$$G = \left(\frac{\gamma^2\tau^2}{\gamma^2\tau^2 B_x^{(static)2}+1}\right), \quad [s5]$$

is sensitive to the static field component, $B_x^{(static)}$. The gain is largest when $B_x^{(static)} = 0$, and if the sensor moves, and the background field magnitude increases, the gain will drop, making the sensor less sensitive to neuromagnetic fields.

To measure the magnitude of this effect, 6 OPM sensors were placed inside the field nulling coil, oriented with their long axes parallel to the field produced by the bi-planar B_z-coil. The background field was nulled as in normal operation. To simulate a neuromagnetic field, small oscillating currents were applied to each of the sensors at known frequencies (131 Hz, 137 Hz, 139 Hz, 141 Hz, 143 Hz and 145 Hz) using the on-board coils. To simulate a changing background field, rather than moving the sensors, the current through the B_z-coil was varied, changing the background field approximately from -1.5 nT to +1.5 nT in 9 sequential steps. This resulted in 9 data segments, in which the small

oscillating field could be measured in the presence of 9 known background fields. We then plotted the amplitude of the simulated neuromagnetic field against the background field.

Extended Data Figure 4a shows example data from a single sensor; the effect of stepping the background field can be seen clearly, and the inset plot shows a few cycles of the 137 Hz oscillating field which mimics neuromagnetic signal. Extended Data Figure 4b shows power spectra of each of the 9 data segments independently, for the same sensor. In the inset graph, note that the magnitude of the 137 Hz peak changes depending on which data segment is studied. Finally, Extended Data Figure 4c shows the fractional change of the oscillating field amplitude as a function of background field. The green line shows a fitted Lorentzian curve (of the form $y = \frac{a}{b(x-c)^2+1} + d$) showing that our data agree with the analytical analysis above (Eq. s5). Error bars show standard deviation over the six sensors. Over the dynamic range of the sensor (±1.5 nT) the gain changes by ~4 %.

Importantly, measurement of the standard deviation of the static field in the six finger abduction experiments was 0.25 ± 0.2 nT when the subject was moving and 0.12 ± 0.04 nT when the subject was stationary. This means that approximately 95 % of our data will experience a gain error of less than 0.5 %. For the purposes of our proof-of-principle demonstration this error was considered acceptable. However, future system modification could take this changing gain into account in data modelling.

7) DISCUSSION: EXPANSION OF THE FIELD NULLING COIL SYSTEM:

The current field nulling coil system has a 40 x 40 x 40 cm^3 volume, within which the error in the uniformity of the field or field gradient generated by the coils is <5 %. Whilst this 'box' (within which the subject can move) is relatively large, some applications may require it to be expanded. Such expansion is readily achievable, with the simplest way being to increase the area of the coil planes and/or reduce their separation relative to their in-plane extent.

The final dimensions of the current coil set were determined practically, by the size and layout of the MSR in which the OPMs were operated. This MSR contains a 275 channel cryogenic MEG system, the presence of which limited the size of the coils to squares of 1.6 m side length (this was the maximum size that could be achieved whilst still allowing the coils to be easily removed from the MSR during liquid cryogen fills and studies using the cryogenic machine). The position of the cryogenic system and its chair also imposed restrictions on the separation of the two planes. The plane-separation of 1.5 m was chosen to allow the coils to be sited around the cryogenic system. The

presence of the chair, positioned in the gap between the coil planes, also meant that the subject had to remain seated during all OPM-MEG experiments.

Coils designed with these limitations produced homogeneous fields, or field gradients, over a central volume which comfortably spans the head and the OPM array. Further, this volume allows for flexible head movement, accommodating a range of potential applications as described in our main manuscript; it certainly provides a more comfortable experience than is possible using a typical cryogenic system where movement is limited to <5 mm. Nevertheless, enhancing the experimental setup to allow a greater range of motion during an OPM-MEG measurement is the ultimate aim for the technology.

Key enhancements of several aspects of the technology will be required before this can be realised. Importantly, the extent of movement would be ultimately limited by the MSR layout. Therefore, it would be advantageous to design an MSR specifically with OPM-MEG in mind. Removing the cryogenic system could allow the subject to stand. It would also allow the use of novel coil designs whose size and separation would be limited only by the dimensions of the MSR, which would readily allow an increase in the size of the homogeneous region. For example, simply doubling the dimensions of the current coils would produce homogeneous fields, or field gradients, over a central volume of 80 x 80 x 80 cm^3 which would immediately allow a much wider range of motions.

Coil designs could also be modified, for example by using the same coil design method, but changing the coils' aspect ratio. This could allow subjects to move around within a 'corridor' or allow multiple subjects to interact with one another. The coils could also be built directly into the walls of the MSR (notwithstanding any interactions between the fields and the mu-metal that would need to be taken into account in the design process) lessening any restrictions the coils would impose on the range of movements available to the subject. Also, here only the field and first order spatial field gradient terms have been considered. Designs could also be extended to produce higher order field terms in order to provide further reduction of the remnant field inside the MSR.

The ability of the bi-planar coils to generate controlled patterns of spatial magnetic field variation could be exploited to measure the positions and orientations of the OPM sensors, providing the information needed for data modelling. In the current system, this information is provided by the scanner cast, however in future systems, following further miniaturisation of OPMs, one could envisage smaller OPMs held in a flexible 'cap' (similar to EEG). Removing the requirement for a scanner cast would be advantageous in terms of both practicality (no need for 3D printing or MRI)

and cost. However, use of such a system would require a way of determining the sensors' locations and orientations relative to each other, and to the brain. Application of a known (e.g. sinusoidal) current to the bi-planar B_x, B_y and B_z coils, and subsequent measurement of the ratios of the amplitudes of the fields measured at the sensors to the applied fields, would yield orientation information for every sensor. Similarly, the spatial positions of the sensors (relative to each other) could be found by analysing the fields measured when known currents are applied to the gradient coils. These methods, coupled with the use of a set of fiducial coils placed at anatomical landmarks (similar to current cryogenic MEG) would give complete information on the OPM montage and its location relative to the head

8) A COMPARISON WITH ELECTROENCEPHALOGRAPHY

Electroencephalography (EEG) involves measurement of the electrical potentials generated at the scalp surface by the same neural current flow that gives rise to the MEG signals[7]. The lightweight nature and flexibility of placement of the EEG electrodes means that EEG constitutes a wearable brain imaging system. There is no reason why OPM-MEG and EEG data could not be captured at the same time (e.g. with EEG electrodes placed between OPM sensors). However EEG alone also notionally offers direct competition to the wearable OPM-MEG system described here. For this reason, we undertook a direct comparison of EEG and OPM-MEG.

Data collection and analysis:

To facilitate a comparison between EEG and OPM-MEG data, we undertook two sets of experiments:

1. The finger abduction experiments reported in the main manuscript were repeated, while EEG data were collected. A single experiment comprised 50 trials, each involving 1 s of finger abduction and 3 s rest. 50 'dummy' trials were interleaved. The subject who previously participated in the OPM-MEG study, undertook the experiment 12 times, 6 where they kept as still as possible, and 6 where they made natural head movements during the task. Head motion was measured using the Xbox Kinect camera, which tracked movement of a single head marker. These experiments were directly equivalent to those undertaken using OPM-MEG and reported in Figure 2.
2. Previous publications[8-10] have suggested a difference in the manifestation of muscle artifacts (unwanted signals generated at scalp sensors due to electrical activity in muscles around the head and neck) between MEG and EEG. To investigate such artifacts, we ran the same finger abduction paradigm (50 trials, 1 s movement, 3 s rest), but asked the subject to tense the muscles in their jaw and neck during the movement period (as well as move their finger) so as to produce task-correlated muscle artifacts. This experiment was repeated twice, once with data recorded with OPM-MEG, and once with data recorded using EEG.

In the above experiments, EEG data were acquired using BrainAmp MRplus EEG amplifiers (Brain Products, Munich) with a 1 kHz sampling rate and a frequency range of 0.06-250 Hz (30 dB roll-off at high frequencies). A standard 63-channel EEG cap (EasyCap, Herrsching) was fitted to the subject by an experienced EEG user, with electrode impedances maintained below 10 kΩ for the duration of the study (these were checked regularly between data recordings). The electrode layout followed the extended international 10-20 system with an additional channel for recording the electrocardiogram (ECG). FCz was used as the reference electrode during acquisition. All data were acquired using BrainVision Recorder software (v1.2, Brain Products, Munich). The spatial separation of EEG electrodes on the scalp was 2.9 ± 0.3 cm, which was similar to the spatial separation of OPMs in our OPM array (2.2 ± 0.2 cm).

EEG data were initially analysed in BrainVision Analyzer2. For each experiment, data were visually inspected for noisy channels; only electrode Tp10 was found to be noisy (in 2/13 recordings) and was excluded (in these 2 runs). Data were referenced to an average of all remaining channels to provide as clean a reference signal as possible (with minimal neuronal or artifactual signals[11]). Following this, data were exported to Matlab where a sensor space analysis was carried out.

For each EEG sensor, a time-frequency spectrogram (generated using a Hilbert transform – see Materials and Methods) was employed to visualise the neural oscillatory response to finger movement. An equivalent sensor space analysis was undertaken of the OPM-MEG data. In all cases, baseline oscillatory amplitude, computed in the 3 s < t < 3.5 s time window, was subtracted so that time-frequency spectra showed absolute change from baseline. For the muscle-tensing paradigm, quantitative analysis was carried out in the 20 to 55 Hz frequency range; absolute change in oscillatory amplitude from baseline, in the 0.25 s < t < 1 s time window (during the muscle clench), was normalised by the baseline estimate to assess fractional change in amplitude. EEG and OPM-MEG results were compared.

Results

Extended Data Figure 5a shows results of the muscle tensing paradigm. Extended Data Figure 5ai shows a visualisation of the 64-channel EEG montage using the extended 10-20 system (top) alongside the 21-channel OPM-MEG montage used to assess muscle artifacts (bottom). Extended Data Figure 5aii shows time-frequency spectra extracted from three channels of interest, again for EEG (top) and OPM-MEG (bottom). Note that these channels (indicated by the red stars in Extended Data Figure 5ai) were selected because they showed the largest beta band response to finger abduction

in separate experiments. Notice that, for OPM-MEG, although a muscle artifact is observed, the beta response is still clearly visible. However, in the EEG channels, the beta response is completely obscured by the muscle artifact (this was the case in all channels). The bar chart in Extended Data Figure 5aiii shows the size of the muscle artifact (averaged across 13 sensors covering the sensorimotor strip as indicated by the black circles in Extended Data Figure 5ai) relative to baseline. Note that the size of the artifact in EEG is ~10 times larger than the equivalent artifact in OPM-MEG. For completeness we also measured the size of the artifact relative to the beta rebound (the only phase of the beta response still visible in the EEG data). This was done for the three (MEG and EEG) channels shown in Extended Data Figure 5aii. In EEG, the artifact was 31 ± 4 times larger than the rebound. In MEG this value dropped to 2 ± 1.

Extended Data Figure 5b shows a direct comparison of EEG and OPM-MEG data recorded during the finger abduction task. For both modalities, data from a single sensor with the largest beta band fluctuation (for data recorded in the static case) has been chosen for visualisation. Movement data, recorded using the X-box Kinect camera, are also shown. The left-most two time-frequency spectra show data averaged over all six experiments (300 trials), whereas the right-most two time-frequency spectra show a single representative experiment (50 trials). Both finger abduction and resting trials are shown. With the head static, OPM-MEG and EEG offer similar results at the channel level; the expected beta modulation is shown clearly whilst higher frequencies, and resting trials show no obvious fluctuations. However, with the head freely moving, whilst OPM-MEG data show a clear response, EEG data suffer from significant artifact generated by muscle activity (as well as, potentially, movement degrading the contact of the electrode with the scalp). Whilst averaging over more trials (300 compared to 60) reduces the contribution of muscle artifact to the processed EEG signal, it does not eliminate it. Results therefore show clearly that EEG data, acquired in a freely moving subject, does not produce the same quality of neuronal responses as that afforded by OPM-MEG.

Discussion: The advantages of OPM-MEG over EEG

The advantages of OPM-MEG over EEG can be broken down into three areas, 1) sensitivity to muscle artifact; 2) spatial resolution and 3) practical issues. These are discussed below.

Muscle artifacts

The results above show that muscle artifacts in EEG and MEG begin in the low beta band (~15-20 Hz) and extend into the higher (gamma) frequency range. This result is in good agreement with previous findings: for example, Whitham et al.[12] recorded EEG data with and without neuromuscular

blockade, with results showing that EEG data are contaminated at frequencies above ~20 Hz. Our data also show that EEG is markedly more sensitive to such artifacts than MEG. Again this is not a new finding[8-10], and it occurs because the magnetic field falls off rapidly as distance to the primary dipole generator increases, whereas volume conduction in EEG facilitates greater (and less predictable) spatial spread of the measured electrical potential.

Muscle artifacts are clearly an issue in a wearable neuroimaging system, particularly during paradigms (such as those employed in the present paper) where head and face movement is either expected or task related. Given its lower sensitivity to muscle artifacts, MEG offers significant advantages in this area. Crucially however, in standard MEG systems this benefit has not been realised due to the fixed nature of cryogenic equipment and thus EEG is the current go-to modality for wearable monitoring of neuronal activity[13]. The primary neuroscientific applications of wearable neuroimaging include scanning babies and toddlers; elderly patients with movement disorders; paradigms with free head movement (e.g. spatial navigation) and 3D virtual reality. In all of these cases, muscle artifact would be a big concern. Further, clinically, a useful application of wearable neuroimaging is in epilepsy: it is widely acknowledged that the ictal discharge initiates an epileptic seizure and that the site of this discharge is an appropriate target for surgical resection, however such events are often obscured in EEG by associated muscle artifact[14]. It therefore follows that OPM-MEG technology, with its reduced artifact sensitivity, offers a distinct advantage over EEG for clinical and neuroscience-focused studies.

Spatial Resolution

Beyond muscle artifacts, there are other significant advantages to the use of OPM-MEG over EEG, with perhaps the most obvious being the increased spatial specificity. Indeed, this was eloquently highlighted in a recent review[15] which explained that EEG signals are strongly affected by the substantial difference in electrical conductivity between the scalp, skull, brain, and other biological tissues. The extra-cranial magnetic fields are much less sensitive to these variations in tissue conductivity. Consequently, the spatial topography of MEG sensor data is less smeared and distorted than that of EEG electrical potentials produced by the same physiological sources. This contributes to a clearer interpretation of MEG sensor topography. Further MEG has more accurate forward models (due to the low complexity of these models relative to EEG), which, in turn, improves the accuracy of inverse modelling resulting in a better spatial resolution of MEG compared to EEG.

Practicalities

Finally OPM-MEG offers a number of practical benefits above and beyond EEG. EEG electrodes must be placed in electrical contact with the head – in our experiments contact is maintained using a conductive gel placed between the electrode and the scalp. Use of abrasive gel is also often required to remove dead skin cells and grease from the scalp in order to limit the contact impedance of the electrode. The fact that each electrode must be treated separately in this regard makes EEG set-up time long. The process can also be uncomfortable for the subject and may not be tolerated by some subject groups. OPM-MEG set-up time on the other hand is relatively short since no electrical contact is required. The requirement for electrical contact also raises other potential issues: electrical contact between electrodes via the conductive gel (bridging) is undesirable since it acts to spatially blur the measured spatial topography, but can be difficult to avoid in high density EEG studies. This is not a problem for OPM-MEG (where sensor cross-talk can be controlled). OPM-MEG also potentially offers greater scan-to-scan consistency between experiments in the same subject. This is because whilst the sensitivity of OPMs does not change between experiments, the sensitivity of EEG is dependent on the quality of connection to the scalp (hence there exists a subject and operator dependency). It also means that long-term (12-24 hour) OPM recordings could be considered without any concerns regarding data quality (due to impedance changes). Finally, in clinical studies, OPMs, being contactless, reduce any risks of infection and for studies following surgery (for example in epilepsy) recordings could be made through bandages (which is impossible using EEG).

9) EXAMPLE APPLICATION: BRAIN CONNECTIVITY MEASUREMENT

The last decade has seen a paradigm shift in neuroimaging[16], from the study of discrete functional regions to the identification of networks in which individual (functionally specific) brain regions work in concert. The primary finding is that spontaneous brain activity, measured in the 'resting state' (i.e. in the absence of a task) contains robust spatio-temporal signatures, which define a number of distributed networks, some associated with sensory processing (e.g. the motor network) and others with attention or cognition (e.g. the default-mode network)[17]. A great deal of evidence shows that these networks, and the connectivities that define them, are key to healthy brain function and are altered in many pathologies. However, despite huge progress in this area, little is known about how these brain networks develop throughout childhood and adolescence. Some insights have been gathered using functional magnetic resonance imaging (fMRI)[18], however this only gives an indirect measure of brain 'activity' based on blood flow, and so misses the key electrophysiological effects that underpin connectivity (i.e. neural oscillations). Some insight could be gained using electroencephalography (EEG), however this lacks the spatial specificity to characterise network

signatures, and is further compromised in young children whose skulls have not yet fused. With whole brain coverage, direct access to electrophysiology and good spatial resolution, MEG is the method of choice for measurement of electrophysiological connectivity, however in conventional systems scanning subjects younger than ~8 years old is difficult due to small head size. Further younger subjects often fail to keep still, again confounding data collection. It follows that OPM-MEG, with the flexibility to place OPMs directly on the scalp, and a wearable system in which subject can move freely, offers a unique opportunity to characterise the developing human connectome.

Measurement of functional connectivity offers a significant challenge to any neuroimaging system. In traditional neuroimaging experiments, data are collected whilst the subject performs the same task many times across a large number of trials; these trials are then averaged to increase the signal to noise ratio (SNR). However, in assessment of resting state functional connectivity there are no trials, and functional connectivity must be inferred using unaveraged data. A high fidelity system with excellent SNR is therefore critical. In addition to demonstrating direct applicability, demonstration of functional connectivity measurement using an OPM-MEG system also therefore offers an opportunity to test data quality.

Methods:

The array of OPM sensors was expanded, from 13 to 26. A new scanner cast was also constructed; again an MRI scan was used to define the outer surface of the subject head, but unlike our somatosensory cast (where the positions of the OPM slots were based on a-priori MEG data), here OPM slots were distributed evenly over the whole head (81 slots were fabricated in total). Our 26 OPM sensors were configured to cover the left and right parietal lobes. (Note that expanded coverage and more sensors, relative to our 13 channel array, was necessary for connectivity experiments, since we require measurement of the interaction between spatially separate regions.) The sensor coverage of our 26 channel array is shown in Extended Data Figure 6a.

The subject was placed in the scanner-cast and asked sit still with their eyes open and ‘think of nothing’. To maintain fixation, a red cross on a grey background was presented to the subject via projection on a screen. 300 s of OPM-MEG data were acquired (with field nulling identical to that previously described). This experiment was repeated twice.

Data were frequency filtered to the beta band and reconstructed in source space at the vertices of a regular 4 mm grid spanning the whole brain, using the beamformer spatial filter (see Materials and Methods). A seed location of interest was defined anatomically in the hand area of left primary motor cortex. A seed-based connectivity analysis was then undertaken in which statistical interdependency

between the seed timecourse and all other 'test' timecourses (i.e. all other voxels in the brain) was computed[19]. The major confound of such analyses is that, due to the ill-posed nature of the MEG inverse problem, spatially separate regions may exhibit dependency between source timecourses purely as a result of the inherent spatial smoothness of the beamformer reconstruction – this is termed signal leakage[20]. To avoid this problem, a regression technique was used to remove any linear projection of the seed timecourse on all possible test timecourses. Previous demonstrations[19,21] show that this technique significantly reduces the leakage confound. Following leakage reduction, the seed and test timecourses were subjected to Hilbert transformation to yield the analytic signal. The absolute value of the analytic signal was then calculated to obtain the amplitude envelope of beta band neural oscillations. In accordance with previous literature[19,22], these envelopes were then smoothed temporally (to an effective time resolution of 1 s) and Pearson correlation between the seed envelope, and all possible test envelopes was computed. Finally, this procedure was repeated for the theta (4-8 Hz), alpha (8-13 Hz), low gamma (30-50 Hz) and high gamma (50-100 Hz) frequency bands in order to assess the spectral signature of functional connectivity.

Results

Extended Data Figure 6b-d show the results of our connectivity analysis. Extended Data Figure 6b shows the voxels exhibiting the strongest functional connectivity with the seed location (red/yellow overlay); the seed is shown by the blue circle. As would be expected, strong functional connectivity is observed in the homologous area of right hemisphere, showing clearly a well delineated sensorimotor network. Extended Data Figure 6c shows the spectral signature of functional connectivity between the left and right motor regions, with a clear peak in the beta frequency band; again this is exactly as expected given previous demonstrations[17,19,22]. Finally, Extended Data Figure 6d shows the reconstructed smoothed beta band oscillatory envelope data (temporally down-sampled to 1 s); the left sensorimotor cortex (seed location) is shown in blue and the right sensorimotor cortex in red. Note that the statistical interdependency between these two spontaneously measured signals can be seen clearly. These data show that, even in a single subject and with just 26 channels, our system was able to collect high fidelity (unaveraged) data, sufficient in quality to allow functional connectivity metrics to be evaluated. Measurement of the developing human connectome is currently an expanding area of research (see e.g. http://www.developingconnectome.org) and our system offers a means by which network connectivity could be measured in babies, children, adolescents and adults, capturing key developmental milestones: for example sensorimotor network connectivity and dynamics could be measured as a child learns to walk; or the language network could be imaged as a child learns to talk – such metrics are extremely challenging with conventional MEG. Finally, little is known about network dynamics when subjects (children or adults) undertake natural movements

in an unconstrained way (e.g. the ball game paradigm in Figure 4). Our system, for the first time, has the potential to investigate such processes.

10) CROSSTALK BETWEEN OPM SENSORS

A potential concern in the operation of an OPM scalp sensor array is that nearby OPMs may interfere with each other. Specifically, the oscillating modulation field is applied with the same amplitude, frequency and phase at all sensors. If two sensors, A and B (see Extended Data Figure 8a) are placed in close proximity, the cell in sensor A will not only see its own modulation field, but also that of sensor B. These two modulation fields will interfere, meaning that both the gain and sensitive orientation of sensor A may be modulated simply by the presence of sensor B, and vice versa. Here, using both simulations and experiments, we attempted to examine the magnitude of this effect.

Simulation

The known geometry of the on-board sensor coils (i.e. the coils that generate the modulation field) was used to produce a physically accurate discrete element model (N = 360 current elements) of each coil. The Biot-Savart law was used to calculate the magnetic field, at each sensor location, from each current element, and the fields from all elements were summed. In the present OPM array, we only measured neuromagnetic field components radial to the head - therefore only the radial coils were used for modulation and our simulations consider this arrangement. The coil currents were set to an arbitrary constant value (0.35 μA giving a 200 pT field in the centre of the cell on which the coil was mounted). Using a 3D digital model of the scanner-cast, the locations and orientations of the sensor slots were determined, and the location of the sensor cell was taken to be the centre of the 3 x 3 x 3 mm^3 cell which was assumed to have a stand-off distance of 6 mm from the end of the sensor casing (and the scalp surface). Sensors were simulated at all 13 slots in the scanner-cast.

For every sensor pair in the array, we computed the relative field strength of the perturbing sensor (A) to the base sensor (B): i.e. if the field from coils in sensor A in cell B is $\boldsymbol{B}_{perturb}(\boldsymbol{r})$, and the field from coils in sensor B in cell B is $\boldsymbol{B}_{base}(\boldsymbol{r})$, we computed

$$\rho(\boldsymbol{r}) = \frac{|\boldsymbol{B}_{perturb}(\boldsymbol{r})|}{|\boldsymbol{B}_{base}(\boldsymbol{r})|} \quad . \qquad [s6]$$

Here, $\boldsymbol{r}$ represents the location of the base sensor cell. These strengths of interaction were used to generate a 13 x 13 matrix which offers a complete characterisation of crosstalk across the 13 sensor array.

It is noteworthy that the ratio is a periodic function, with respect to rotation of the perturbing sensor about its radial axis (i.e. rotation marked by the green arrow in Extended Data Figure 8a). For this reason both the minimum and maximum values of this function were computed and plotted as two separate crosstalk matrices. Simulation results are given in Extended Data Figure 8b, which shows the minimum sensor interaction and Figure 8c which shows the maximum sensor interaction. Crosstalk, as would be expected, is largely a function of sensor proximity, with adjacent sensors demonstrating the largest effects. In the present array, the maximum crosstalk between sensors is around 3 %.

Experimental verification

We set up the scanner-cast with 13 sensors as in Figure 1d but with no subject present. Each sensor has a continuous calibration setting, which outputs a current through its radially- oriented coil, producing a sinusoidal field of amplitude 0.5 nT and frequency from 130-150 Hz. By turning on the continuous calibration on each sensor sequentially, and taking a 2 minute recording of magnetic fields from all sensors, peaks in the power spectral density of all of the sensors were generated corresponding to the strength of the stray field from the perturbing sensor. By dividing the maximum height of the stray field peaks by the height of the peak of the sensor producing the varying field we enabled estimation of the relative strength of crosstalk, as a measure directly comparable to that in Eq. s6. The experimental results, which are shown in Extended Data Figure 8d, agree with those obtained through simulation.

Both simulation and experiment implied that in the worst case, crosstalk between sensors in our 13 sensor array corresponded to a change in modulation field of approximately 3 %. For the purposes of the present demonstration, this small change was deemed acceptable and was therefore ignored in the measurements presented in Figures 2 and 4. (In the 26 channel array used in our connectivity demonstration, sensor separation is larger and therefore these effects were also assumed to be negligible.) However, it is worth noting that with higher density sampling (e.g. for an OPM-MEG system with hundreds of channels) where sensors must be sited closer to one another, these effects will worsen. In addition, recording tangential, in addition to radial, fields may also cause a worsening of crosstalk. For this reason, crosstalk will need to be treated carefully in future work, and for high density arrays we expect that such effects will need to be eliminated, e.g. by taking them into account in forward field modelling.

11) INTERFERENCE FROM MUSCLE ARTIFACT – REDUCTION IN MEG

SI section 6 shows that muscle artifacts are significantly (around 10 times) worse in EEG compared to OPM-MEG. Nevertheless, it also shows that these artifacts are present in the OPM-MEG data, and it is critical to demonstrate ways to ameliorate this problem. This is of particular importance for wearable MEG, where subject motion is not only possible, but encouraged. The effect of muscle artifacts in MEG data can be reduced in a number of ways. For example, one could use independent component analysis applied at the sensor level[23] (though this potentially poses problems if muscle artifact is task-correlated). Alternatively one can use electrodes, or reference OPMs to measure the electro- or magneto-myogram and then regress these signals from the measured MEG data (though this requires a more complex experimental set up with sensors placed close to all muscle groups thought to pose a problem). Such methods are never perfect and obviously the higher the amplitude of the artifact, the greater the residual effect following 'correction'. Here, we used an adaptive beamformer spatial filter to remove this artifact.

Although classically thought of as a mechanism for source localisation, the adaptive beamformer is also a powerful means to remove artifacts from MEG data[24,25]. As noted in the Materials and Methods section, the fundamental premise of the beamformer is that weights are derived to minimise the variance of the output signal whilst maintaining signals originating at some location of interest in the brain. This means that sources with spatial topographies that resemble dipoles in the brain will remain, whilst sources whose topographies could not originate from the activity in the brain (such as muscle artifacts) will be supressed.

To demonstrate this, we recorded OPM-MEG data during the finger abduction paradigm (50 trials, 1 s movement, 3 s rest), but asked the subject to tense the muscles in their jaw and neck during the movement period. Note that this represents a worst possible case scenario, where the subject tenses all of their muscles in the face and neck, time-locked to the paradigm.

These data were analysed in three ways. First, we employed a beamformer spatial filter to look at a location of interest in the right sensorimotor region. The beamformer data covariance was computed in the 10-50 Hz frequency band and using a time-window spanning the entire experiment (all 400 s). No regularisation was applied. Second, an overly-regularised beamformer was applied (with the regularisation parameter equal to 100 times the maximum eigenvalue in the unregularized matrix). The effect of this over-regularisation is seen clearly in Equation 6, since in a case where $C \ll \mu\Sigma$, the equation for the beamformer weights collapses to $\mathbf{W}_{\theta\_reg}^{T} = \left[\mathbf{L}_{\theta}^{T}\mathbf{L}_{\theta}\right]^{-1}\mathbf{L}_{\theta}^{T}$; i.e. the weights become a

scaled version of the lead fields, and the beamformer solution becomes analogous to a dipole fit. Finally, a single sensor, with the largest beta band response was selected. For all three analyses, we constructed time-frequency spectra showing the oscillatory amplitude change averaged across trials.

Results are shown in Extended Data Figure 10. Extended Data Figure 10a shows the montage of OPM-MEG channels employed to measure data. Extended Data Figure 10b shows a beamformer image, highlighting a location of interest in right sensorimotor cortex. Panel c shows the time-frequency response for the best OPM-MEG sensor, whilst panel d shows equivalent time-frequency spectra, reconstructed at the location of interest identified in panel b. The left hand panel of d shows the over-regularised beamformer reconstruction; the right hand panel shows the unregularized beamformer reconstruction. Note that a large muscle artifact, overlapping with the beta response to finger movement, is clear in the best sensor and over-regularised beamformer data. However, following beamforming, the power minimisation ensures that the artifact is effectively reduced in magnitude. This example shows that even in a bad case, where high-amplitude, task-correlated muscle artifacts contaminate the data, those artifacts are readily controlled. Whilst beamforming is not the only solution to this problem, this example, in agreement with previous literature[24-26], shows it to be a highly effective one.

REFERENCES

1 Brookes, M. J. *et al.* Investigating spatial specificity and data averaging in MEG. *NeuroImage* **49**, 525-538 (2010).

2 Liuzzi, L. *et al.* Optimising experimental design for MEG resting state functional connectivity measurement. *NeuroImage* **In submission** (2016).

3 Hamalainen, M. S., Hari, R., Ilmoniemi, R. J., Knuutila, J. & Lounasma, O. V. Magnetoencephalography: Theory, instrumentation, and applications to non-invasive studies of the working human brain. *Reviews of Modern Physics* **65**, 413-497 (1993).

4 Stevenson, C. *et al.* Does function fit structure? A ground truth for non-invasive neuroimaging. *NeuroImage* **94**, 89-95 (2014).

5 Shah, V. & Romalis, M. V. Spin-Exchange-Relaxation-free Magnetometrty Using Elliptically Polarised Light. *Physical Review A* **80**, 013416 (2009).

6 Tannoudji, C., Dupont-Roc, J., Haroche, S. & LaLoe, F. Diverses résonances de croisement de niveaux sur des atomes pompés optiquement en champ nul i. théorie. *Revue de physique appliquee* **5** (1970).

7 Berger, H. Über das Elektrenkephalogramm des Menschen. *Archiv für Psychiatrie und Nervenkrankheiten* **87**, 527-570 (1929).

8 Claus, S. C., Velis, D., Lopes da Silva, F. H., Viergever, M. A. & Kalitzin, S. High frequency spectral components after Secobarbital: The contribution of muscular origin-A study with MEG/EEG. *Epilepsy Research* **100**, 132-141 (2012).

9 Muthukumaraswamy, S. D. High-frequency brain activity and muscle artifacts in MEG/EEG: a review and recommendations. *Frontiers in Human Neuroscience* **7**, 138 (2013).

10 Zimmermann, R. & Scharein, E. MEG and EEG show different sensitivity to myogenic artifacts. *Neurol Clin Neurophysiol.* **78** (2004).

11 Mullinger, K. J., Mayhew, S. D., Bagshaw, A. P., Bowtell, R. & Francis, S. T. Poststimulus undershoots in cerebral blood flow and BOLD fMRI responses are modulated by poststimulus neuronal activity. *Proc Natl Acad Sci U S A* **110**, 13636–13641 (2013).

12 Whitham, E. M. *et al.* Scalp electrical recording during paralysis: quantitative evidence that EEG frequencies above 20 Hz are contaminated by EMG. *Clin. Neurophysiol.* **118**, 1877-1888 (2007).

13 Kranczioch, C., Zich, C., Schierholz, I. & Sterr, A. Mobile EEG and its potential to promote the theory and application of imagery-based motor rehabilitation. *International Journal of Psychophysiology* **91**, 10-15 (2014).

14 Sardouie, S. H., Shamsollahi, M. B., Albera, L. & Merlet, I. Denoising of Ictal EEG Data Using Semi-Blind Source Separation Methods Based on Time-Frequency Priors. *IEEE Journal of biomedical and health informatics* **19**, 839 (2015).

15 Baillet, S. Magnetoencephalography for brain electrophysiology and imaging. *Nature Neuroscience* **20**, 327–339 (2017).

16 Raichle, M. A Paradigm Shift in Functional Brain Imaging. *Journal of Neuroscience* **29**, 12729-12734 (2009).

17 Brookes, M. J. *et al.* Investigating the Electrophysiological Basis of Resting State Networks using Magnetoencephalography. *Proceedings of the National Academy of Science USA* **108**, 16783-16788 (2011).

18 Grayson, D. S. & Fair, D. A. Development of large-scale functional networks from birth to adulthood: A guide to the neuroimaging literature. *NeuroImage* **S1053-8119(17)30102-7**, doi: 10.1016/j.neuroimage.2017.1001.1079. [Epub ahead of print] (2017).

19 Hipp, J. F., Hawellek, D. J., Corbetta, M., Siegel, M. & Engel, A. K. Large-scale cortical correlation structure of spontaneous oscillatory activity. *Nature Neuroscience* **15**, 884-890 (2012).

20 O'Neill, G. C., Barratt, E. L., Hunt, B. A. E., Tewarie, P. K. & Brookes, M. J. Measuring electrophysiological connectivity by power envelope correlation: A technical review on MEG methods. *Physics in Medicine and Biology* **60**, R271-R295, doi:10.1088/0031-9155/60/21/R271 (2015).

21 Brookes, M. J., Woolrich, M. W. & Barnes, G. R. Measuring Functional Connectivity in MEG: a Multi-Variate Approach insensitive to linear Source Leakage. *NeuroImage* **63**, 910-920 (2012).

22 Brookes, M. J. *et al.* Measuring Functional Connectivity Using MEG: Methodology and Comparison With fcMRI *NeuroImage* **56**, 1082-1104 (2011).

23 Escudero, J., Hornero, R., Abásolo, D., Fernández, A. & López-Coronado, M. Artifact removal in magnetoencephalogram background activity with independent component analysis. *IEEE Trans Biomed Eng.* **54**, 1965-1973 (2007).

24 Brookes, M. J. *et al.* Optimising experimental design for MEG beamformer imaging *NeuroImage* **39**, 1788-1802 (2008).

25 Sekihara, K., Nagarajan, S. S., Poeppel, D. & Marantz, A. Performance of an MEG adaptive-beamformer source reconstruction technique in the presence of additive low-rank interference. *IEEE Trans. Biomed. Eng.* **51**, 90-99 (2004).

26 Brookes, M. J. *et al.* Source localisation in concurrent EEG/fMRI: Applications at 7T. *NeuroImage* **45**, 440-452 (2009).

Extended Data Figures

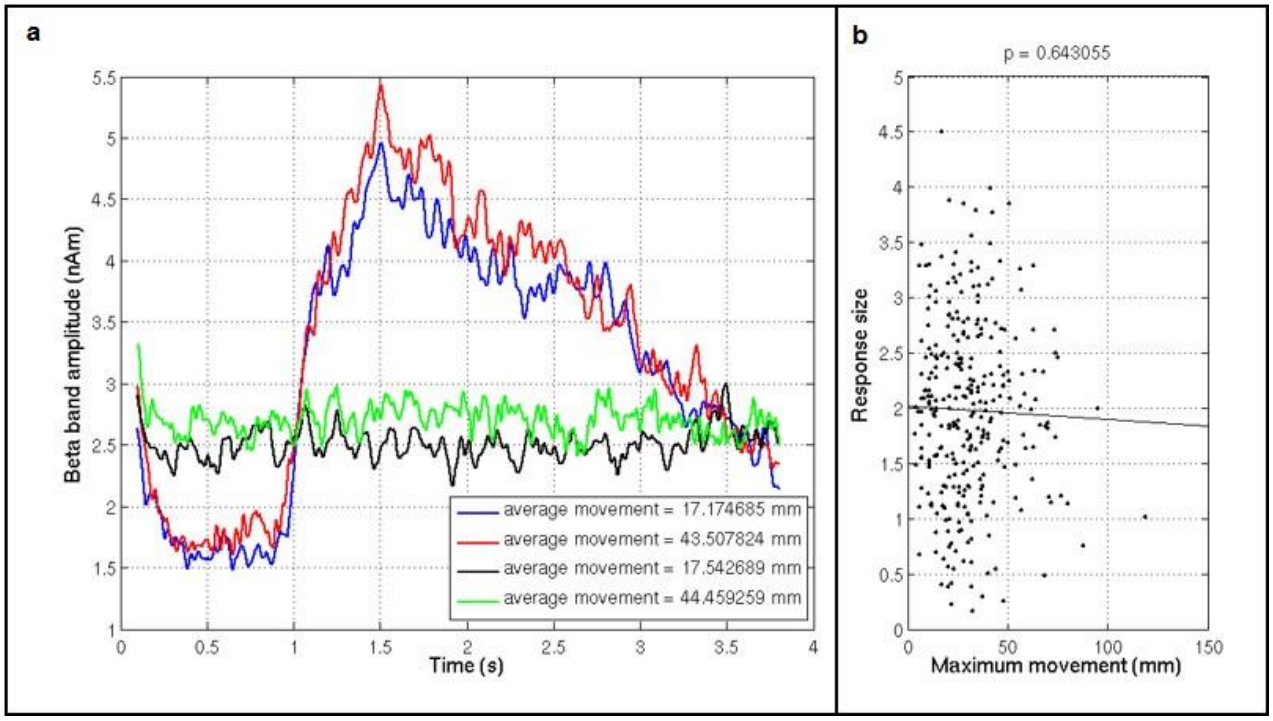

Extended Data Figure 1: Response magnitude as a function of subject movement. *a) Beta envelopes for finger abduction trials (blue/red) and resting trials (black/green) in the presence of large movement (red/green) and small movements (blue/black). b) The response size (i.e. the difference between the mean amplitude during the desynchronization and rebound periods) shown as a function of maximum movement during a trial. Note that no measurable relationship was found. A significant ($p<0.05$) baseline shift was observed in both the finger-abduction and rest trials; this is likely to be a consequence of artifacts in the data generated by electrical activity in muscles controlling the naturalistic movements.*

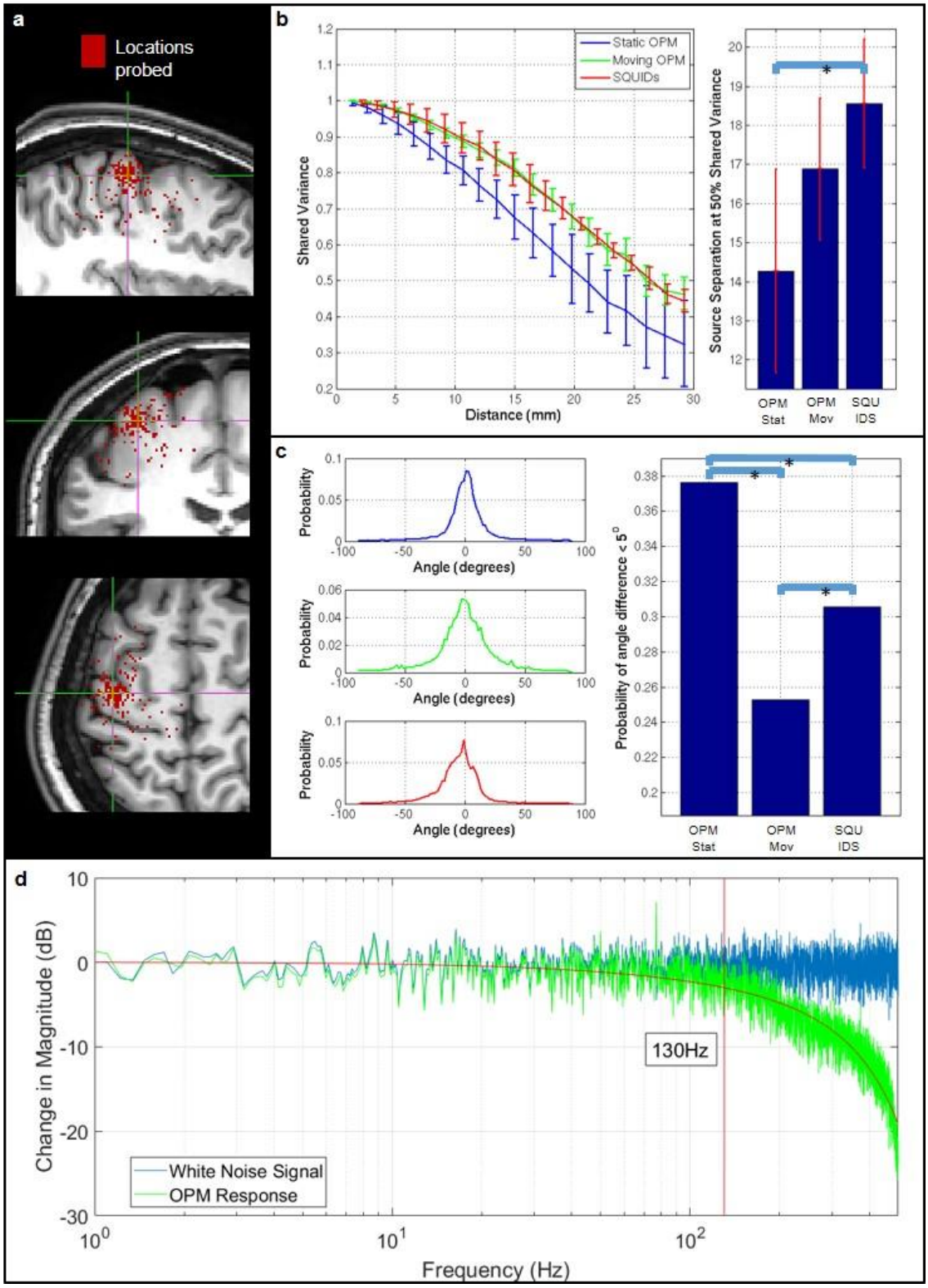

Extended Data Figure 2: Quantification of spatial and temporal resolution. *a) A 'seed' location was selected in sensorimotor cortex (at the cross-hairs). 4000 random 'test' locations, within 3 cm of the seed, were selected randomly and probed. Shared variance was measured between electrophysiological timecourses at the seed and test locations. b) The line graph shows correlation between the seed and test timecourses plotted as a function of spatial separation. The bar chart shows the source separation at which shared variance dropped to <50 %. In both cases the error*

bars show standard deviation over test locations. This serves as an absolute quantification of spatial resolution. Note that the OPM array, when static, significantly outperforms SQUIDs ($p < 0.05$). c) Quantification of the robustness of the source orientation estimation. Whilst source power can vary between experiments, source orientation relies only on the local orientation of the cortical sheet, and should therefore be the same across equivalent experiments. Here the histograms show the source orientation difference (as an angle) across runs for 4000 locations of interest. Note for all three experiments (static OPMs (top) moving OPMs (middle) and SQUIDs (bottom)) the probability distribution peaks at zero as would be expected. The bar chart shows the probability of observing an angular discrepancy < 5 degrees; note that the OPM array, when static, significantly ($p < 0.05$) outperformed the SQUID array in terms of orientation robustness. Moving OPMs demonstrated the lowest robustness, however this would be expected since the execution of natural movements differed across runs and therefore brain activity in the sensorimotor strip will also differ. The improvement in spatial specificity and robustness in our OPM-MEG system compared to a cryogenic (SQUID) system is likely a consequence of two things – first, the closer proximity of the OPM sensors to the scalp provides higher signal to noise ratio in OPMs compared to SQUIDs; second, the scanner cast ensures that, for each run, OPM sensors are in exactly the same location with respect to the brain. Cryogenic MEG, on the other hand, is subject to coregistration errors. d) Quantifies the OPM sensor's frequency response which also defines its temporal resolution. An OPM sensor was placed in a Helmholtz coil and a white noise current source applied to the coil. The blue line shows the Fourier spectrum of the current source, the green line shows the spectrum of the measured field. Note that sensitivity falls by 3 dB at 130 Hz, giving a temporal resolution of 7.7 ms.

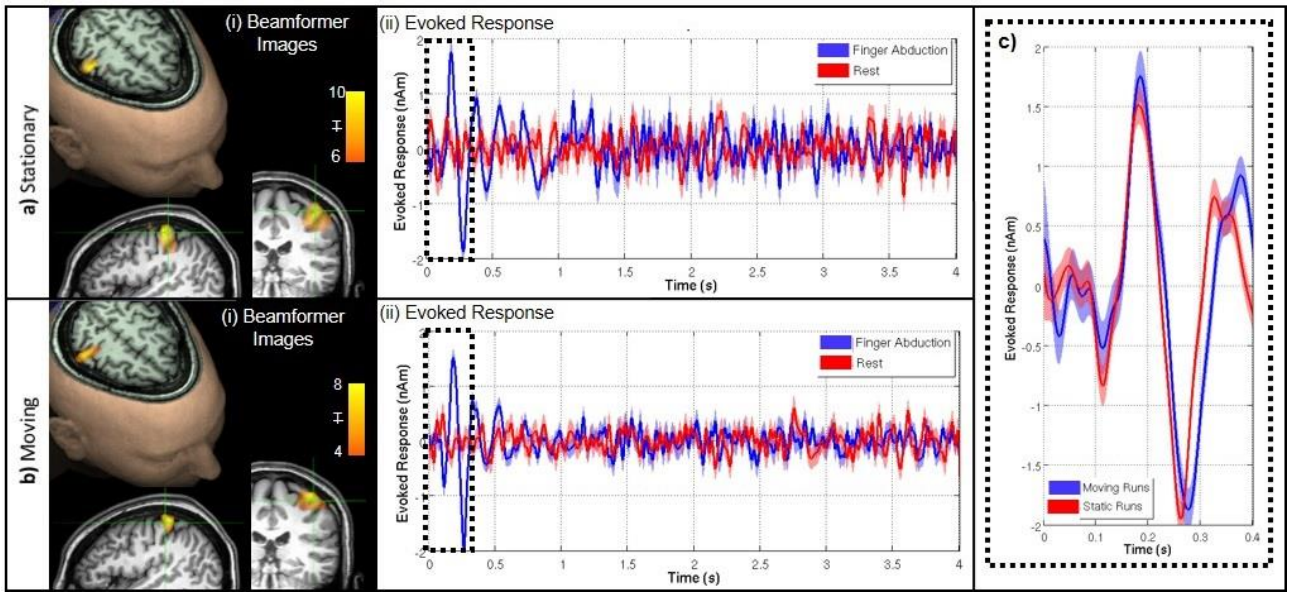

Extended Data Figure 3: Evoked response analysis. *a) Shows the case when the subject was asked to remain still, b) shows the case when the subject was moving. i) Functional image: the overlay shows the spatial signature of the 2-30 Hz component of the evoked response, overlaid onto axial, sagittal and coronal slices of the anatomical MRI. ii) The time course of the evoked response; finger abduction trials in blue, rest trials in red. The shaded area shows standard error across 6 experiments. c) Direct comparison of the evoked response in the case where the subject was asked to remain still (red) and was moving (blue). No significant SIR difference was found between static and moving runs.*

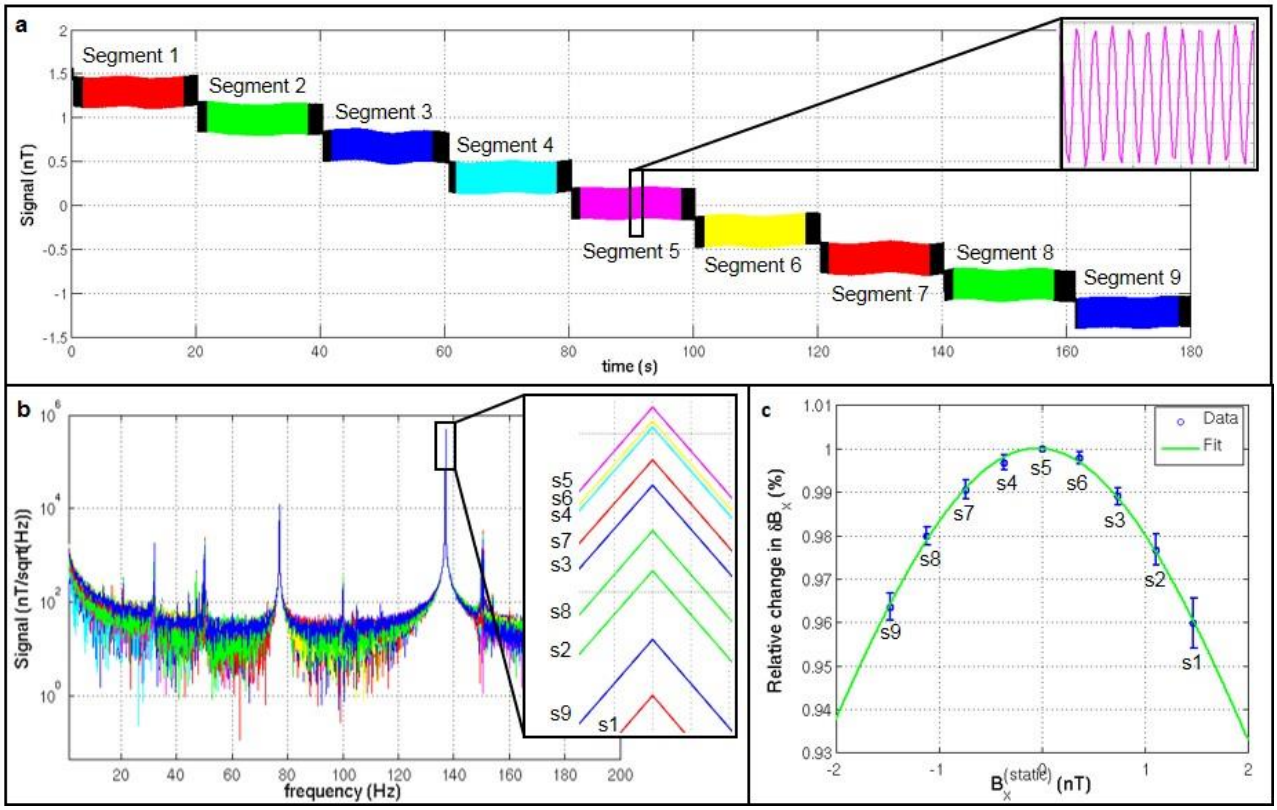

Extended Data Figure 4: Gain changes with static magnetic fields. *a) Raw OPM-MEG data recorded from a single channel during the gain experiment. Data were divided into 9 segments (colour-coded here) corresponding to 9 different static background magnetic fields ($B_x^{(static)}$), ranging between -1.5 nT and 1.5 nT. The inset plot shows the small oscillating field (δB_x), applied (in this sensor) at 137 Hz using the radially oriented on-sensor coil, that mimics neuromagnetic activity. b) Fourier transforms of each data segment. The inset figure shows the height of the 137 Hz peak for different segments. Note that the peak height changes as a function of static magnetic field. c) Fractional change in δB_x as a function of background field $B_x^{(static)}$. The blue circles show the measured data with the standard deviation over the six sensors. The green line shows a fitted Lorentzian function.*

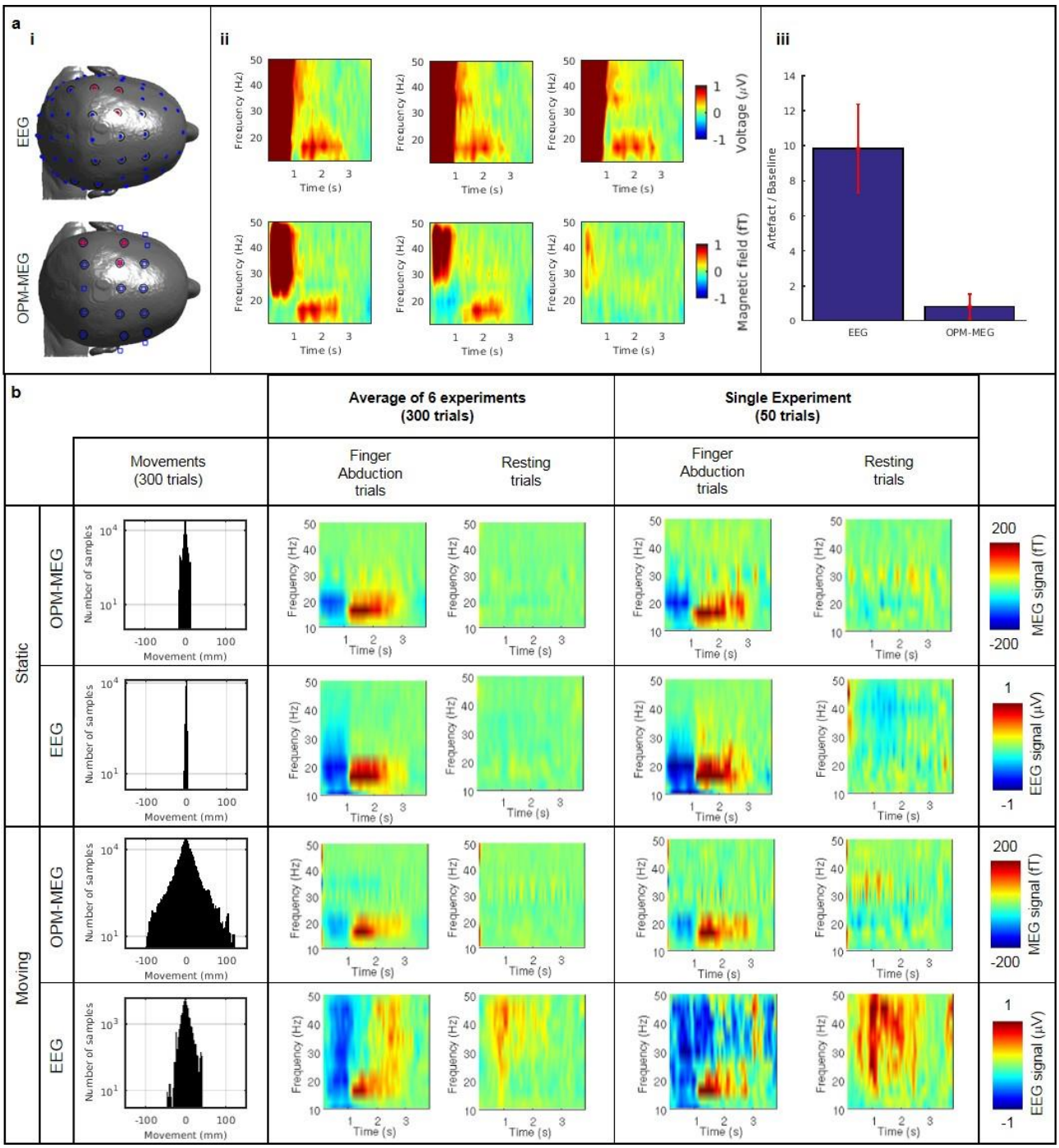

Extended Data Figure 5: A comparison of EEG and OPM-MEG. a) Muscle tensing experiment. *i) Channel montages for EEG (top) and OPM-MEG (bottom). Blue circles show EEG channels used; blue squares show MEG channels used; red stars denote channels used to create (ii); black circles indicate channels used for averages in (iii). ii) Time-frequency spectra showing fractional change in oscillatory amplitude, relative to baseline. The three plots show three separate channels, with the muscle artifact visible in the 0-1 s window, when jaw clenching took place. iii) Quantitative analysis of the magnitude of the artifact, which was measured to be ~10 times larger in EEG. Error bars show standard deviation across sensors.* ***b) Finger abduction experiment.*** *The 4 separate rows show OPM-MEG and EEG data with the subject stationary, followed by OPM-MEG and EEG data with*

the subject making natural movements. The left-hand column shows movement parameters. The left and left-centre time-frequency spectra show absolute difference from baseline of the MEG (in fT) and EEG (in μV) signals for individual channels, in the finger abduction and resting trials, respectively. These results have been averaged across all six experiments in both modalities. The right and right-centre time-frequency spectra show equivalent visualisations for a single representative experiment. Notice that, with the head static, MEG and EEG show similar results. However with the head moving, EEG data suffer from artifact generated by muscle activity, to which the MEG data are less susceptible.

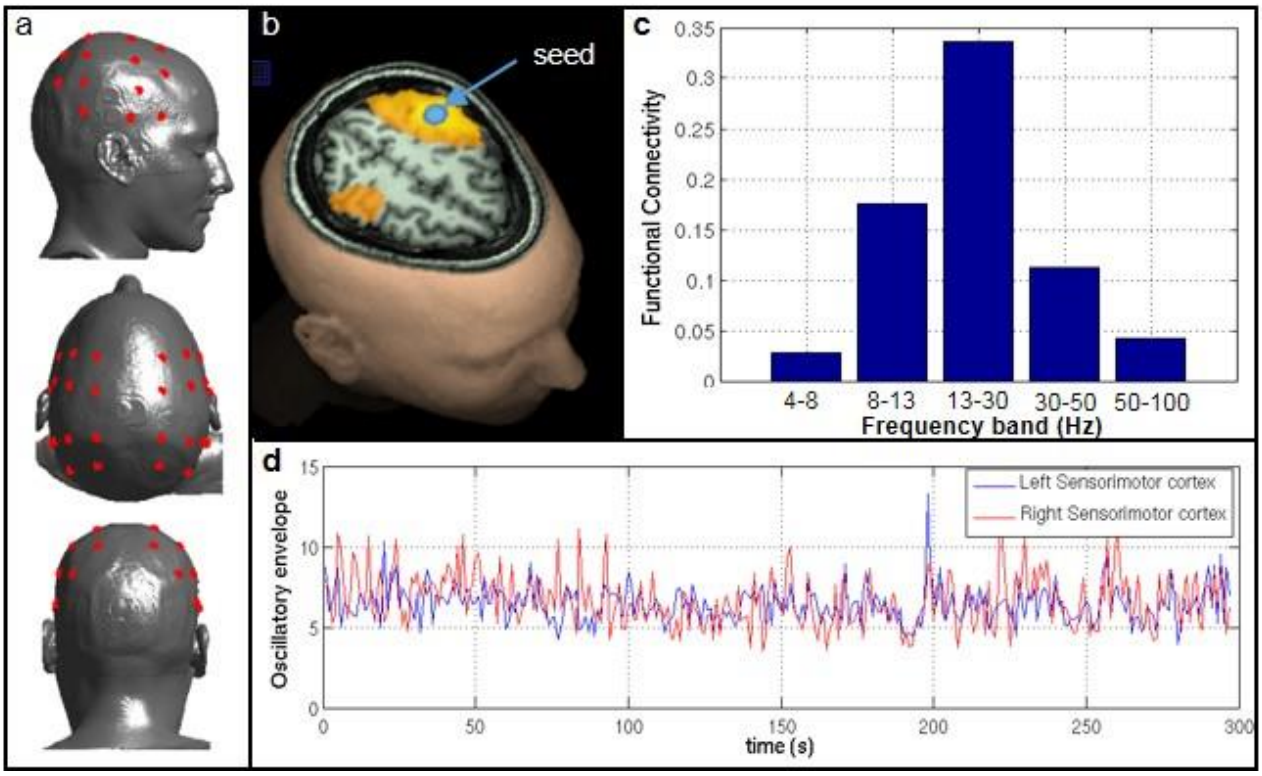

Extended Data Figure 6: OPM-MEG derived functional connectivity. *A single subject took part in an experiment in which 5 minutes of OPM-MEG data were acquired in the resting state (subject was told to 'think of nothing'). The experiment was repeated twice and the results averaged. a) A 26 channel OPM scalp array, with OPM sensors positioned (using a scanner cast) approximately to cover the left and right parietal lobes (red circles in a). MEG data were reconstructed in source space using a beamformer, on a 4 mm grid covering the entire brain. A seed location was selected in left sensorimotor cortex and functional connectivity between the seed and the rest of the brain computed using an amplitude envelope correlation measurement, with correction for signal leakage by regression. b) Regions exhibiting strongest functional connectivity to the seed location (in the beta frequency band). Note that, in addition to a region around the seed, functional connectivity is observed in the homologous regions of the opposite hemisphere. This reflects long range functional connectivity within the sensorimotor network. c) Functional connectivity strength between left and right primary sensorimotor cortex, plotted as a function of frequency. Note that, as expected, functional connectivity between these regions is greatest in the beta band (13-30 Hz). Finally, d) shows an example of beta band envelopes from the left (blue) and right (red) sensorimotor cortices, derived from resting state data.*

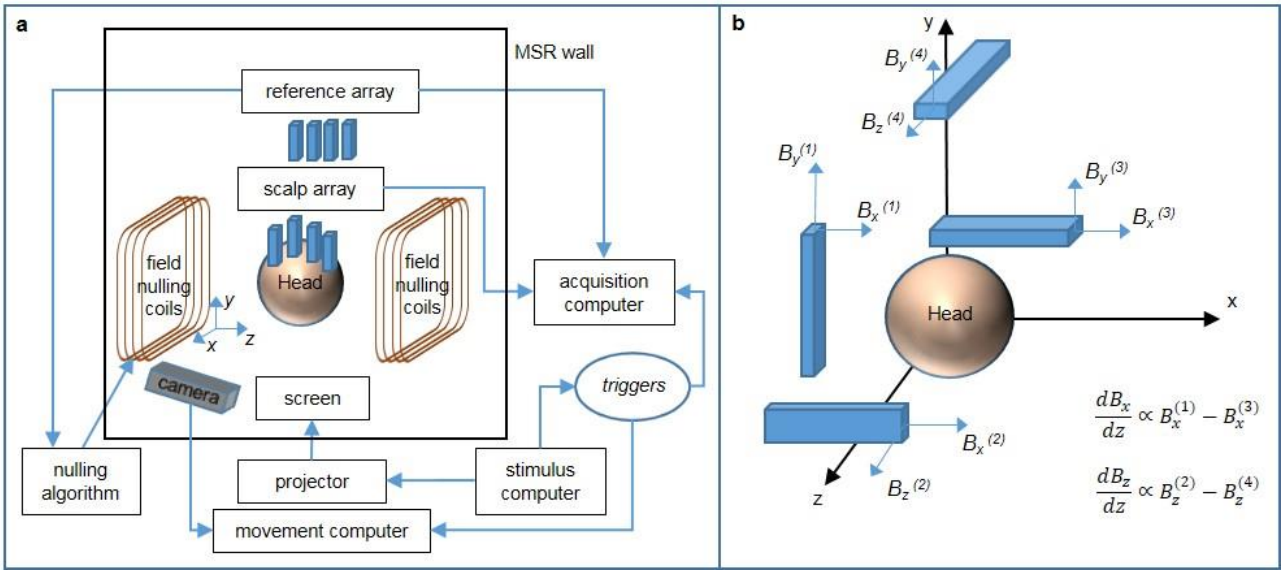

Extended Data Figure 7: An overview of the OPM-MEG system *a) Schematic diagram showing an overview of system hardware. b) Positioning of the reference sensors relative to the head to allow measurement of the three Cartesian components of the magnetic field, and the two dominant spatial gradients of the field. Each sensor provides measurements of two components of the magnetic field that are perpendicular to the beam axis. Both components were measured for field nulling, but during experimental measurements only the component of the field along the long-axis of the sensor was measured.*

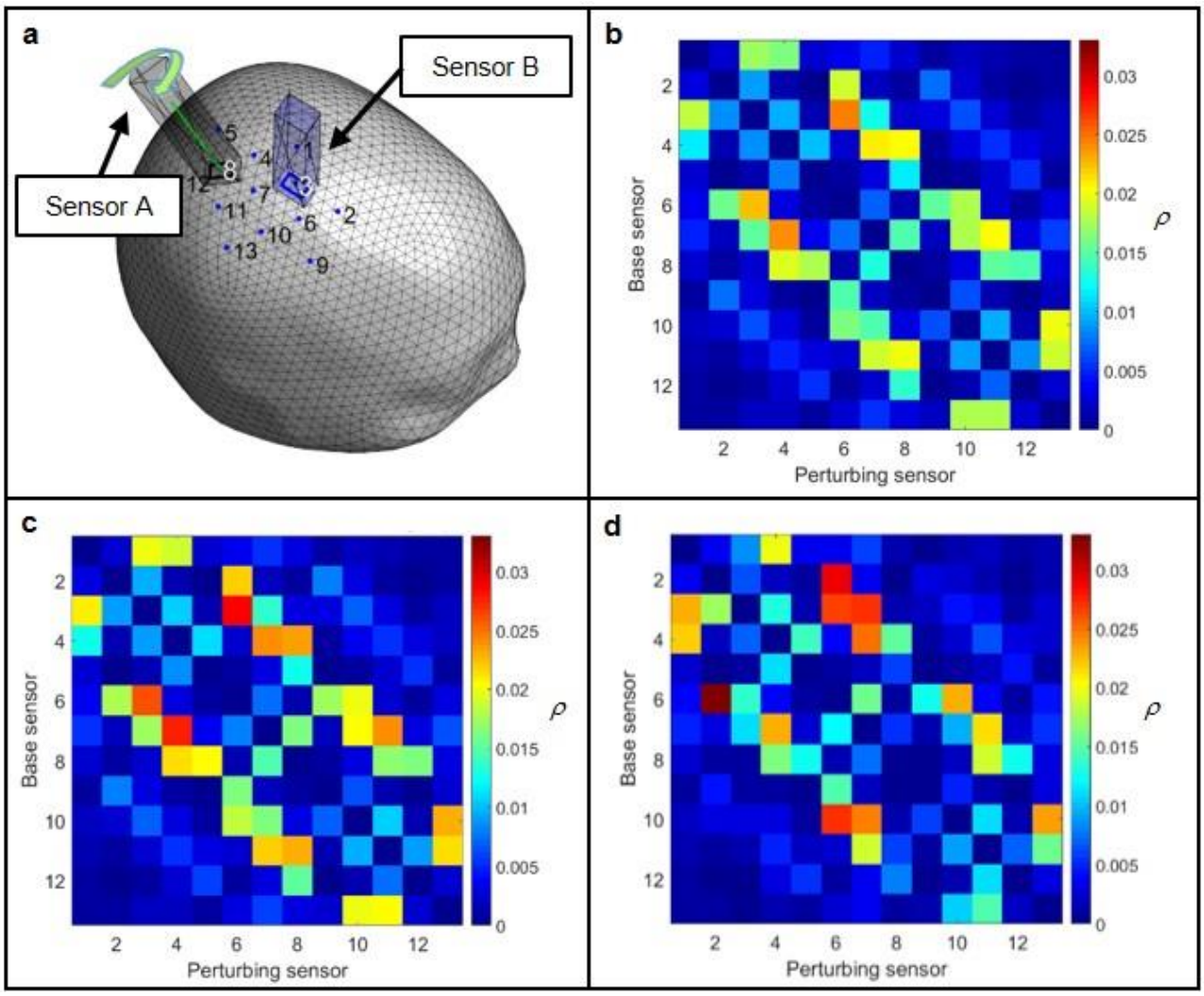

Extended Data Figure 8: Crosstalk characterisation across an OPM array. *a) Schematic 3D representation of the crosstalk simulation. The head surface is shown alongside two example sensors. The locations of all 13 sensors are also indicated. We sought to characterise crosstalk between all pairs of sensors in the array. b,c) Simulated crosstalk between sensors measured as the ratio of fields generated by the perturbing sensor and the base sensor at the position of the base sensor. This ratio is a periodic function of sensor rotation about the radial orientation, the minimum interaction is shown in b, the maximum is shown in c. d) Experimentally measured crosstalk matrix.*

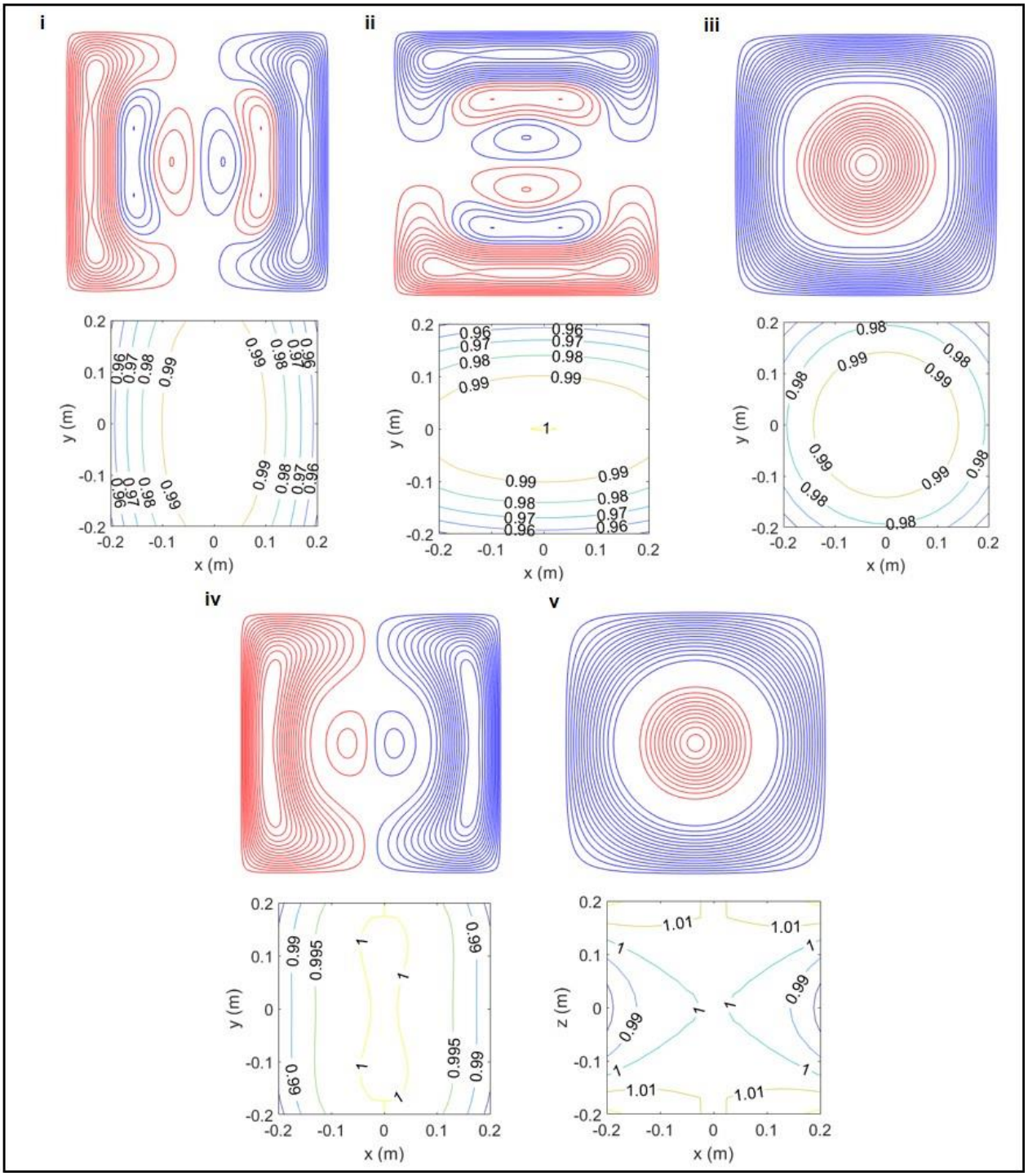

Extended Data Figure 9: Coil designs. *Wire paths and field plots are shown for the five coils: i) B_x ii) B_y iii) B_z iv) dB_x/dz v) dB_z/dz. The upper portion of each sub-figure shows the wire paths for one (1.6 x 1.6 m^2) plane of the bi-planar coil. Red and blue colours indicate clockwise and anti-clockwise circulation of the current. The lower portion shows contours of the field or field gradient strength over the 0.4 x 0.4 m^2 x – y plane located at the centre of the volume of interest (z=0) (For (v) contours are shown in the x – z plane at y=0). The field or gradient values are normalised to the value at x=y=z=0. Variation from the ideal field distribution are less than 5 % over a 0.4 x 0.4 x 0.4 m^3 central volume.*

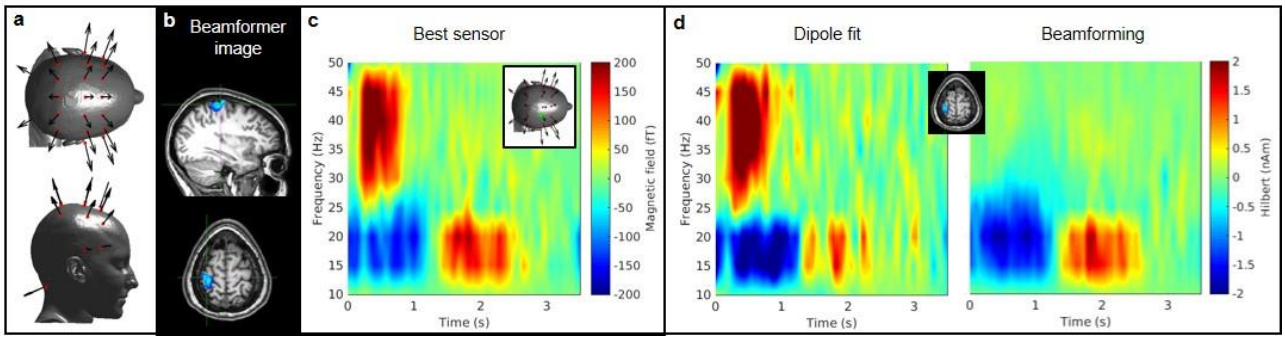

Extended Data Figure 10: Removal of muscle artifacts via beamforming. *a) The montage of OPM-MEG channels employed to measure muscle artifact data. b) A beamformer image, highlighting a location of interest in right sensorimotor cortex. c) The time frequency response for the best OPM-MEG sensor. d) Reconstructed responses from the over-regularised beamformer (which is analogous to dipole fitting) (left) and un-regularised beamformer (right). Note that for un-regularised beamforming the muscle artifact is supressed effectively.*